Additive Manufacturing 22 (2018) 852–868

Contents lists available at ScienceDirect

Additive Manufacturing

journal homepage: www.elsevier.com/locate/addma

Full Length Article

Fast prediction of thermal distortion in metal powder bed fusion additive manufacturing: Part 1, a thermal circuit network model

Hao Peng[a,1], Morteza Ghasri-Khouzani[b], Shan Gong[b], Ross Attardo[c], Pierre Ostiguy[c], Bernice Aboud Gatrell[c], Joseph Budzinski[c], Charles Tomonto[c], Joel Neidig[d], M. Ravi Shankar[b], Richard Billo[e], David B. Go[a,f,*], David Hoelzle[g,**]

[a] Dept. of Aerospace and Mechanical Engineering, University of Notre Dame, United States
[b] Dept. of Industrial Engineering, University of Pittsburgh, United States
[c] Johnson & Johnson Co., United States
[d] ITAMCO, United States
[e] Dept. of Computer Science, University of Notre Dame, United States
[f] Dept. of Chemical and Biomolecular Engineering, University of Notre Dame, United States
[g] Dept. of Mechanical and Aerospace Engineering, The Ohio State University, United States

ARTICLE INFO

Keywords:
Additive manufacturing
Powder bed fusion
Direct metal laser sintering
Thermal distortion
Thermal stress
Thermal circuit network

ABSTRACT

The additive manufacturing (AM) process metal powder bed fusion (PBF) can quickly produce complex parts with mechanical properties comparable to wrought materials. However, thermal stress accumulated during PBF induces part distortion, potentially yielding parts out of specification and frequently process failure. This manuscript is the first of two companion manuscripts that introduce a computationally efficient distortion and stress prediction algorithm that is designed to drastically reduce compute time when integrated in to a process design optimization routine. In this first manuscript, we introduce a thermal circuit network (TCN) model to estimate the part temperature history during PBF, a major computational bottleneck in PBF simulation. In the TCN model, we are modeling conductive heat transfer through both the part and support structure by dividing the part into thermal circuit elements (TCEs), which consists of thermal nodes represented by thermal capacitances that are connected by resistors, and then building the TCN in a layer-by-layer manner to replicate the PBF process. In comparison to conventional finite element method (FEM) thermal modeling, the TCN model predicts the temperature history of metal PBF AM parts with more than two orders of magnitude faster computational speed, while sacrificing less than 15% accuracy. The companion manuscript illustrates how the temperature history is integrated into a thermomechanical model to predict thermal stress and distortion.

1. Introduction

1.1. Problem statement

This manuscript is the first in a two manuscript series (with part 2 found in [1]) describing an algorithm for the fast prediction of thermal distortion in parts printed by the additive manufacturing (AM) process metal powder bed fusion (PBF): also termed direct metal laser sintering and selective laser melting [2]. Metal PBF uses a layer-by-layer build cycle in which at each layer (Fig. 1): 1) a recoater blade spreads a thin layer (20–50 μm) of metal powders at the melt plane; 2) radiant energy is applied to the melt plane by a rastering laser to selectively melt the powder in a two-dimensional (2-D) pattern; and 3) the part is indexed downward to accommodate a new layer of material. In this manner, complex three-dimensional (3-D) parts can be made for relatively low cost in a low-volume production setting (1 – 1000 units) [3]. These capabilities are especially attuned to the low-volume, high value-added aerospace and medical industries [3–13].

Despite the advantages of an increase in permissible part complexity and a decrease in cost at low-volume production, Metal PBF is ultimately challenged by the thermal stresses that develop from the sequence of heat-cool cycles during layer-by-layer melting [14]. In simplest terms, the laser melts metal powder at the melting plane, leading to local thermal expansion of adjacent layers and then followed by local

* Corresponding author at: Dept. of Aerospace and Mechanical Engineering, University of Notre Dame, United States.
** Corresponding author.
E-mail addresses: dgo@nd.edu (D.B. Go), hoelzle.1@osu.edu (D. Hoelzle).
[1] Present address: ITAMCO, United States.

https://doi.org/10.1016/j.addma.2018.05.023
Received 11 October 2017; Received in revised form 19 February 2018; Accepted 12 May 2018
Available online 19 May 2018

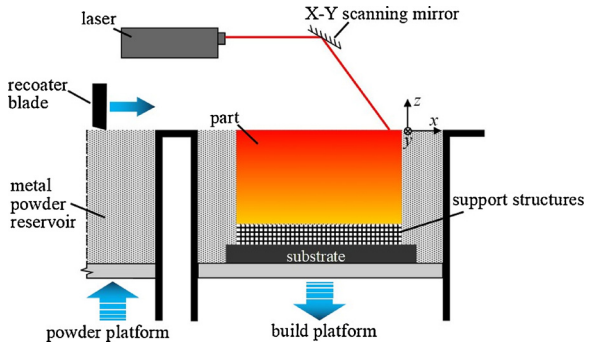

Fig. 1. Schematic of the Metal PBF process.

thermal contraction after the laser passes. As the laser rasters through a layer, and then through subsequent layers, local thermal strains integrate to yield a part with global thermal stress and strain profiles. If the distortion is large enough, the part may be out of specification or, under significant deformation, the recoater blade can crash into the part when passing [15], terminating the build process. Both cases increase waste, driving up cost. Additionally, the temperature history directly affects the local metallurgical phases within a part, influencing both mechanical and corrosion resistance properties [16].

The two most common countermeasures for reducing distortion are proper part build orientation in the machine and the use of sacrificial support structures during the build process [15,17–20]. Both countermeasures change the temperature history of the part, and thus directly affect the distortion profile and part microstructure. Although Metal PBF practitioners have developed orientation and support design heuristics, proper design is not obvious [21]. Accordingly, the economic competitiveness of Metal PBF can be significantly improved by intelligent, automatic algorithms that optimize the build orientation and support design. Almost all design optimization algorithms are iterative [22], requiring the iterative algorithm to solve an objective function composed of the temperature history and distortion prediction on the order of 100 times. Given the stated aim of America Makes and other United States (U.S.) government entities to expand the use of AM [23–25], especially by small businesses with conventional computing resources, each temperature history and distortion prediction must be made on the order of minutes to yield an optimized design on the order of hours.

These two companion papers focus on developing the two computational tools needed to evaluate an objective function for Metal PBF design optimization, temperature history and thermal distortion predictions, on the order of minutes and without the use of computational clusters. This first manuscript defines an efficient temperature history algorithm for Metal PBF. Our method leverages the assumption that the temperature gradient in Metal PBF is largely in the z direction, directed from the melt plane to the substrate; this assumption is supported by previous temperature predictions and observed columnar grains that are preferentially grown in the z direction (shown in Fig. 2(b) and [26–28]). As such, we use geometric relationships between the build layers of a part to determine when horizontal conductive heat transfer can be neglected, thus reducing the number of degrees of freedom in the model while still maintaining fine discretization in the z direction. The algorithm can solve the conductive heat transfer problem during a Metal PBF build with two orders-of-magnitude less computational time than typical finite element method (FEM)-based approaches. To that end, the algorithm meets the need for thermal history prediction on the order of minutes and thus, when coupled with an efficient distortion prediction (as described in the companion manuscript [1]), has the potential to be integrated into a time-efficient design optimization algorithm. Lastly, our approach has a similar motivation as the lumped-parameter models that are ubiquitous to the dynamics systems community for rapid design optimization and control synthesis and have been integrated in to software packages such as MSC Adams and Mathworks Simscape and augment more detailed FEM-based analysis. As Metal PBF advances from expensive trial-and-error studies to advanced process and control design, fast computational models, such as what is described in these two companion manuscripts, will be valuable to augment detailed, FEM-based process analysis.

In this work, we outline the mathematical basis and benchmarking of our new thermal circuit network (TCN) algorithm. The basic strategy is first compared to existing thermal models for metal PBF, and then defined using a simple example in Section 2. Section 3 expands on the simple model, describing the TCN mathematics and algorithm in general. The paper concludes with a case study in Sections 4 and 6 and conclusions and future directions in Section 6.

2. Introduction to the thermal circuit network (TCN)

2.1. Existing metal PBF and direct energy deposition thermal models

This section is intended to outline the general categories of thermal models for PBF and directed energy deposition. Please reference [11–13,29–33] for an exhaustive survey of PBF thermal models.

Existing thermal models of metallic PBF AM almost exclusively use the finite element method (FEM) and can generally be categorized by their domain size and embedded physics [12]. The first category of models simulates the detailed complex physics at the individual powder particle or melt pool level [34–38]. For example, a team at Lawrence Livermore National Laboratory (LLNL) [35] has produced incredibly detailed simulations helping researchers understand the physics of particle migration, capillary flow in the melt pool, and the spatter of the melt due to the recoiling pressure of evaporation. However, there are two limitations of melt pool-scale models. Firstly, the simulation domain is limited to a few millimeters as shown in Fig. 2(a) and (b); secondly, the computational time is prohibitively long, even if high performance computing is used. The second category of models simulate the temperature history in the build of an entire part [39,40] with the domain size ranging from tens to hundreds of millimeters (Fig. 2(c)). To enlarge the domain from only the melt pool to the entire part, the complex physics of Metal PBF must be simplified, often only considering heat conduction [40]. For example, Denlinger et al. [39] performed a thermo-elasto-plastic analysis of the AM process for a large part (3810 × 457 × 25.4 mm). Although they used a layer-by-layer coarsening strategy to reduce the elements used in the lower layers, it took more than 40 h to finish the thermal analysis. Fast computational methods from the company ANSYS-3DSIM require seven minutes to compute temperatures for a part with a 2 mm x 2 mm xy domain [14] and others require an excess of ten hours for an entire part domain (> 5 cm in all directions) [41].

2.2. Preliminaries

The thermal analysis algorithm presented here is considerably different in implementation from standard FEM models. As such, we carefully setup the abstractions, assumptions and the fundamental definitions leveraged in our model. Fig. 3 shows the modeling of AM with different levels of abstraction [42]; here we will take the highest abstraction, sacrificing accuracy for computational efficiency.

- *Abstraction* 1: Adjacent real build layers are modeled as one "*superlayer*", and the deposition of one superlayer represents multiple deposition processes of real build layers. *Justification*: The thickness of a real build layer is about 50 μm, thus requiring a significant computational cost to implement. Furthermore, multiple real build layers are physically merged during Metal PBF; micrographs (upper inset of Fig. 2(b)) show that the melt pool spans approximately 4–8 real build layers [43]. Others have used superlayers of 0.5 mm [44], 1 mm [45], and 2 mm [46] and demonstrated drastic improvements

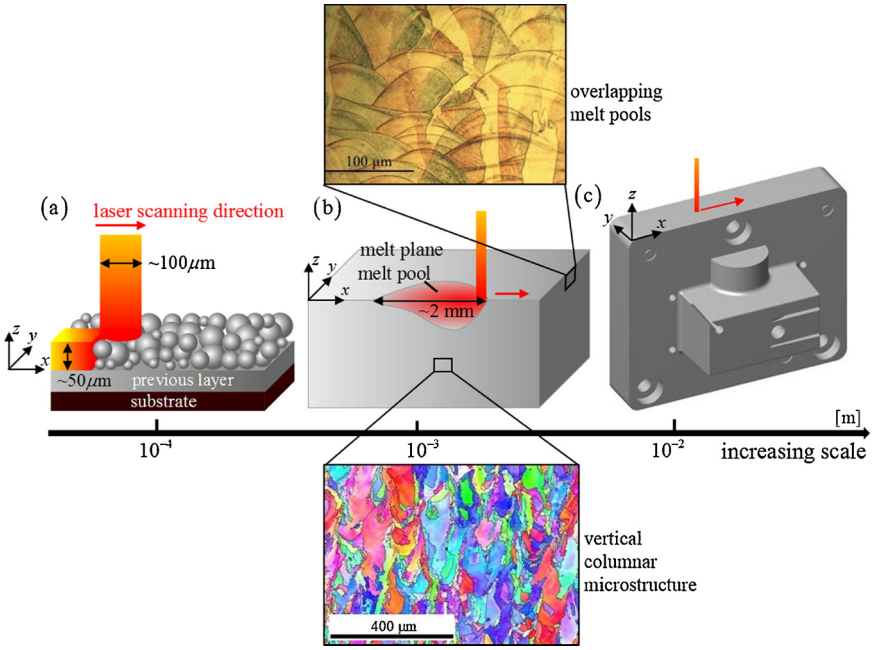

Fig. 2. Metal PBF simulation scales. (a) laser beam scale, (b) melt pool scale (the top inset shows overlapping melt pools observed by surface etching and reflected light microscopy and the bottom inset shows the vertical columnar microstructure observed by electron backscatter diffraction), and (c) part scale.

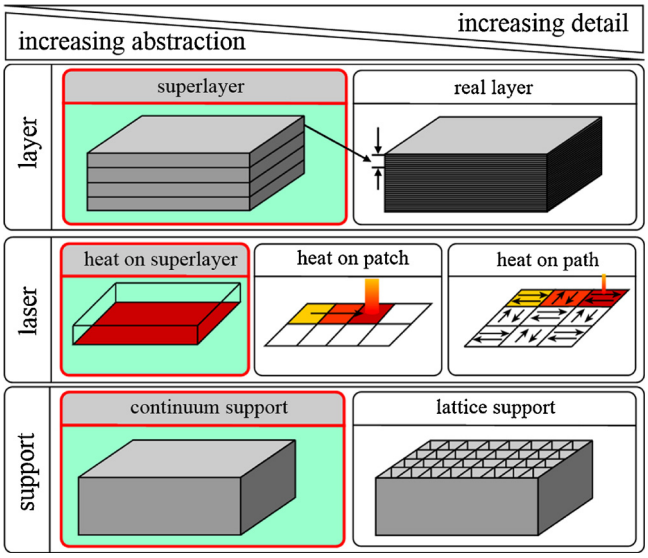

Fig. 3. AM models with different levels of abstraction: abstraction of layer, laser heat input and support structures (motivated by [42]).

in computational efficiency with small changes in computed outputs of distortion and residual stress.

- *Abstraction* 2: The laser beam scanning across the powder bed is modeled as a uniform heat input to each superlayer as opposed to a local laser spot. *Justification*: Because the diameter of the laser beam is about 100 μm, simulating heat transfer at such a small scale prohibits modeling entire parts in a computationally-efficient manner. Furthermore, in the real Metal PBF process, the raster pattern is usually changed in each build cycle (a default of 67° scan direction rotation is used in an EOS machine), and the influence of this laser scanning pattern is averaged out for a superlayer containing multiple real layers. Motivated by [45,47], scan strategy-dependent process artifacts are assumed to be minimized by good process designs used by industrial PBF tools.
- *Abstraction* 3: Supports are modeled as continuum bodies with effective thermal properties without considering the detailed geometries. *Justification*: Support structures, often taking the form of complex lattice geometries [15,19,21,48], can be modeled as simple monolithic bodies with effective material properties. This practice has been employed by [17].

During a real PBF process, heat is transferred through all three modes of heat transfer (conduction, convection, and radiation), but the dominant mode is conduction. We choose to ignore transfer pathways that are an order of magnitude less impactful than conduction through the fused part.

- *Assumption* 1: Radiative and convective heat transfer into the PBF chamber can be neglected. *Justification*: Since the Biot number of parts in Metal PBF is much less than unity (Bi ≈ 0.01 [40]), the convective heat transfer rate is about two orders of magnitude smaller than the conduction rate within the part itself. The radiative heat transfer is high near the melt pool, but the size of the melt pool is negligibly small in comparison to the size of the entire part (Fig. 2(b) and (c)). As such, the total radiative heat transfer is also negligible in comparison to thermal conduction through the entire part and supports. This same assumption has been employed by Roberts [49] and Badrossamay [50].
- *Assumption* 2: Thermal conduction into the powder bed can be neglected. *Justification*: The thermal conductivity of metal powder is only about 2% of the bulk conductivity [51], and hence heat conduction from the solidified metal part into the powder bed is at least one order of magnitude smaller than conduction through the metal part itself.

In summary, based on the above abstractions and assumptions, we model the heat transfer during Metal PBF as an intermittent, uniform heat input to the top-most superlayer and heat is dissipated via conduction through both the previous superlayers and supports to the substrate. We treat the substrate as a constant temperature boundary condition, and all other exposed surfaces as adiabatic boundaries. The laser impinging on the top surface of the top-most superlayer is treated as a volumetric heat source rather than a boundary condition, as discussed in Abstraction 2.

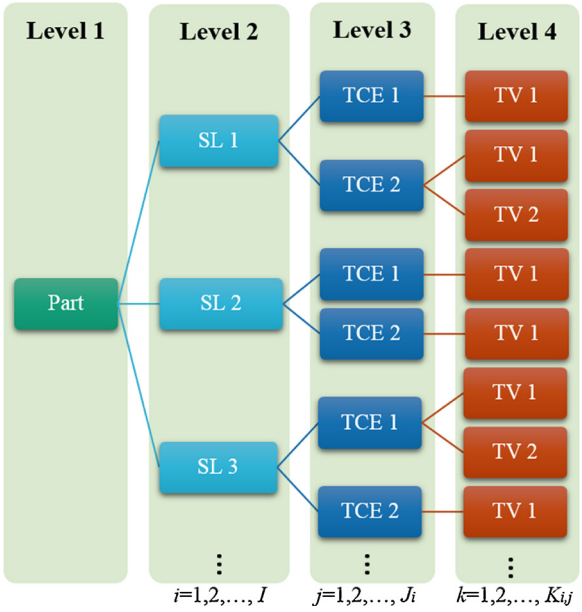

Fig. 4. Representative schematic showing the hierarchy of virtual entities. Level 1 – part, Level 2 – superlayer (SL), Level 3 – thermal circuit element (TCE), and Level 4 – thermal volume (TV).

2.3. Definitions

The definitions set up the terminology and variables used throughout the manuscript. Importantly, we discriminate between real entities that are part of an actual Metal PBF process and virtual approximations to the real entities that are utilized in our TCN model. We also establish a hierarchy of virtual entities as shown in Fig. 4.

Real entities

- *Definition 1: real part*. 3-D volume occupied by the part that is printed.
- *Definition 2*: *real build cycle*. Layer-by-layer build cycle described in the introduction.
- *Definition 3: real build layer*. Layers with thickness ~50 μm deposited in each build cycle of the real Metal PBF build process.

Virtual entities

- *Definition 4: part*. Level 1 in the hierarchy; largest unit of volume of the virtual model.
- *Definition 5: superlayer (SL)*. Level 2 in the hierarchy; virtual superlayer, typically representing multiple real build layers. During a simulated Metal PBF build cycle, a single superlayer, indexed by i, is virtually added to the part such that over multiple cycles, this superlayer-by-superlayer process leads to a total of I superlayers ($i = 1, 2, \ldots, I$). For each virtual build cycle, the superlayer is virtually heated by a laser, which is treated as a uniform heat input, and subsequently virtually cooled.
- *Definition 6: thermal circuit element* (*TCE*). Level 3 in the hierarchy; virtual thermal network of sub-volumes of a superlayer. During a simulated build cycle, a superlayer is added to the part and simultaneously divided into a set of TCEs. TCEs are indexed by the variable j and there are J_i TCEs in the ith superlayer ($j = 1, 2, \ldots, J_i$). Each superlayer retains their TCE architecture throughout the entire virtual build process.
- *Definition 7: thermal volume* (*TV*). Level 4 in the hierarchy; smallest unit of volume in the virtual model and is assumed to have a uniform temperature throughout the volume. Each TV stores thermal energy and has a thermal flow driven by the temperature gradient in relation to adjacent TVs. If in the top-most superlayer, the radiant energy of the laser acts as a heat source to the TV. TVs are indexed by the variable k and there are $K_{i,j}$ TVs in the jth TCE of the ith superlayer ($k = 1, 2, \ldots, K_{i,j}$).
- *Definition 8: virtual build cycle*. Virtual process of building the part superlayer-by-superlayer.

2.4. Introduction to the TCN

We first construct the general form of the TCN equations. These equations will be complemented with a simple example in Section 2.5 and then generalized in Section 3.2. The basic hierarchy and assemblage of the TCN is best illustrated by first considering conservation of energy at the level of a TCE consisting of one or multiple TVs (level 3 of the hierarchy nested with elements of level 4 of the hierarchy). The TV temperatures in the TCE can be assembled into a simple vector of the form $\mathbf{T}_{i,j} = [T_{ij1},\ T_{ij2},\ \cdots,\ T_{ijK_{i,j}}]^T$, and conservation of energy can be written generally as

$$\mathbf{C}_{i,j}\frac{d\mathbf{T}_{i,j}}{dt} = \mathbf{\Omega}_{i,j}\mathbf{T}_{i,j} + \widetilde{\mathbf{Q}}_{i,j} + \mathbf{P}_{i,j} \tag{1}$$

Here, $\mathbf{C}_{i,j}$ is a diagonal matrix containing the TV thermal capacitances $\mathbf{C}_{i,j} = diag(C_{ij1},\ C_{ij2},\ \cdots,\ C_{ijK_{i,j}})$, and $\mathbf{\Omega}_{i,j}$ is a symmetric matrix that describes the thermal conductance between TVs within the TCE (that is, the intra-TCE heat transfer). The second heat transfer term $\widetilde{\mathbf{Q}}_{i,j}$ reflects heat transfer across the boundaries of the TCE – either to adjacent TCEs (inter-TCE heat transfer) or to the substrate supporting the entire part. The last term is a vector $\mathbf{P}_{i,j}$ of non-homogenous sources that represent the laser heat flux applied to the TVs in the TCE: $\mathbf{P}_{i,j} = [P_{ij1},\ P_{ij2},\ \cdots,\ P_{ijK_{i,j}}]^T$. Note that the superscript T denotes the transpose operator and the regular T denotes the temperature variable.

From this general framework at the TCE level, it is relatively straightforward to extrapolate to first the superlayer level and then ultimately the part level. At the part level built up to superlayer i, we obtain a $\sum_{a=1}^{i}\sum_{j=1}^{J_a} K_{a,j}$ -sized vector of TV temperature $\mathbf{T}(i) = [\mathbf{T}_1^T,\ \mathbf{T}_2^T,\ \cdots,\ \mathbf{T}_i^T]^T$, where each sub-vector $\mathbf{T}_i$ is the TV temperatures in the ith superlayer, which itself contains the temperature vectors for its constituent TCEs, $\mathbf{T}_i = [\mathbf{T}_{i,1}^T,\ \mathbf{T}_{i,2}^T,\ \cdots,\ \mathbf{T}_{i,J_i}^T]^T$. Conservation of energy for each TV therefore leads to a system of first-order ordinary differential equations (ODEs) that describe heat flow through an entire part built up to superlayer i [52]

$$\mathbf{C}(i)\frac{d\mathbf{T}(i)}{dt} = \mathbf{\Omega}(i)\mathbf{T}(i) + \mathbf{P}(i). \tag{2}$$

Again, each term is an analog to the terms in Eq. (1), but now at the part level. As such, $\mathbf{C}(i)$ is the diagonal matrix of TV thermal capacitances and the hierarchies are

$$\begin{aligned}
&\text{part:}\mathbf{C}(i) = diag(\mathbf{C}_1,\ \mathbf{C}_2,\ \cdots,\ \mathbf{C}_i);\\
&\text{superlayer:}\mathbf{C}_i = diag(\mathbf{C}_{i1},\ \mathbf{C}_{i2},\ \cdots,\ \mathbf{C}_{iJ_i});\\
&\text{TCE:}\mathbf{C}_{ij} = diag(C_{ij1},\ C_{ij2},\ \cdots,\ C_{ijK_{i,j}}).
\end{aligned} \tag{3}$$

Similarly, $\mathbf{P}(i)$ is the laser heat flux vector of non-homogenous source that represent the laser heat flux applied to the TVs:

$$\begin{aligned}
&\text{part:}P(i) = [\mathbf{0}^T,\ldots,\mathbf{0}^T,\ \mathbf{P}_i^T]^T;\\
&\text{superlayer:}\mathbf{P}_i = [\mathbf{P}_{i1}^T,\ \mathbf{P}_{i2}^T,\ldots,\mathbf{P}_{iJ_i}^T]^T;\\
&\text{TCE:}\mathbf{P}_{ij} = [P_{ij1},\ P_{ij2},\ldots,P_{ijK_{ij}}]^T.
\end{aligned} \tag{4}$$

As the laser is incident on just the TCEs of the top superlayer (superlayer index i), $\mathbf{P}(i)$ has a sparse structure and thus $\mathbf{0}$ is an appropriately sized vector of zeros. Notice that the inter-TCE heat transfer has disappeared at this level of the hierarchy as all heat transfer is through conduction between TV nodes up to superlayer i, or exogenously driven heat transfer from the laser through term $\mathbf{P}(i)$. $\mathbf{\Omega}(i)$ defines the conductive heat transfer between the TVs contained within the i

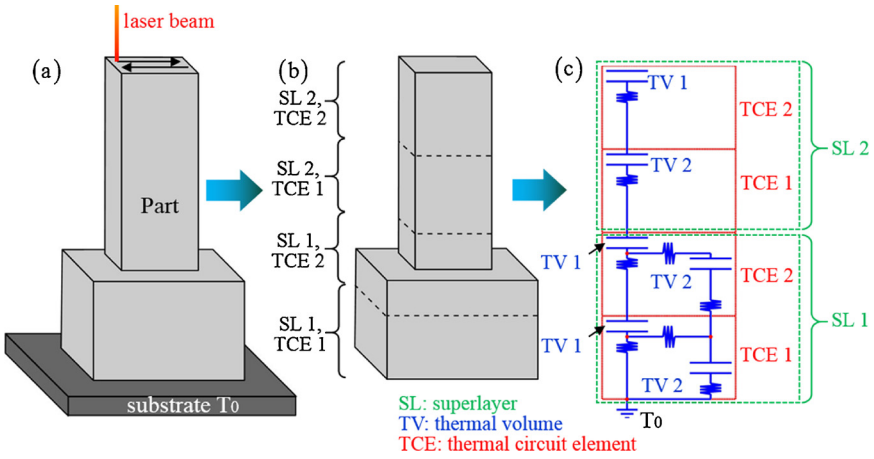

Fig. 5. An illustrative example of the thermal circuit network (TCN) model for the Metal PBF build of a compound rectangular bar. (a) The bar during the Metal PBF build (note that no supports are included). (b) The bar is segmented into SLs, TCEs and TVs. (c) The network of each TCE is assembled into a TCN to model the addition of superlayers during the Metal PBF build.

superlayers; the assemblage of $\mathbf{\Omega}(i)$ is more complicated than Eqs. (3) and (4) and is thus given as a case example in the next section.

2.5. Illustrative example of hierarchical governing equations

To illustrate the hierarchical relationships outlined above, in particular the complicated conductance matrix $\mathbf{\Omega}(i)$, we consider the hierarchical governing equations for a compound rectangular bar as shown in Fig. 5(a). For this illustration, the part is segmented into two superlayers (SLs) and each SL consists of two TCEs (Fig. 5(b) and (c)). The TCEs in the second superlayer each consist of only a single TV. However, in the first superlayer each TCE consists of two TVs. Physically, the connection to the second TVs in these TCEs describes the horizontal heat spread as heat conducts through the larger base of part. Also note that the first (lower) superlayer extends across the interface of the two features, as does the 2nd TCE in the first superlayer. Throughout this example we will omit the assignment of TCN parameters (Ω and C) and simply provide TCN structure; the assignment of parameters is given in Appendix B.

First let us consider the fully assembled part, and the corresponding circuit diagram in Fig. 5(c). With the direct application of conservation of energy to each TV and using the relevant circuit conductances, it is straight forward to construct a set of governing ordinary differential equations for each TV in the thermal circuit of the part and organize them into matrix form as

$$diag\left(\begin{bmatrix}\infty\\ C_{111}\\ C_{112}\\ C_{121}\\ C_{122}\\ C_{211}\\ C_{221}\end{bmatrix}^T\right)\frac{d}{dt}\begin{bmatrix}T_0\\ T_{111}\\ T_{112}\\ T_{121}\\ T_{122}\\ T_{211}\\ T_{221}\end{bmatrix}=\begin{bmatrix}0 & \Omega_{111} & \Omega_{113} & 0 & 0 & 0 & 0\\ \Omega_{111} & A & \Omega_{112} & \Omega_{121} & 0 & 0 & 0\\ \Omega_{113} & \Omega_{112} & B & 0 & \Omega_{123} & 0 & 0\\ 0 & \Omega_{121} & 0 & C & \Omega_{122} & \Omega_{211} & 0\\ 0 & 0 & \Omega_{123} & \Omega_{122} & D & 0 & 0\\ 0 & 0 & 0 & \Omega_{211} & 0 & E & \Omega_{221}\\ 0 & 0 & 0 & 0 & 0 & \Omega_{221} & F\end{bmatrix}\begin{bmatrix}T_0\\ T_{111}\\ T_{112}\\ T_{121}\\ T_{122}\\ T_{211}\\ T_{221}\end{bmatrix}+\begin{bmatrix}0\\ 0\\ 0\\ 0\\ 0\\ 0\\ P_{221}\end{bmatrix},$$

$$\mathbf{C}(2)\frac{d\mathbf{T}(2)}{dt}=\mathbf{\Omega}(2)\mathbf{T}(2)+\mathbf{P}(2) \tag{5}$$

where $A=-\Omega_{111}-\Omega_{112}-\Omega_{121}$, $B=-\Omega_{113}-\Omega_{112}-\Omega_{123}$, $C=-\Omega_{121}-\Omega_{122}-\Omega_{211}$, $D=-\Omega_{122}-\Omega_{123}$ $E=-\Omega_{211}-\Omega_{221}$, and $F=-\Omega_{221}$. For each term, Ω_{ijk} denotes the conductance of the kth resistance of the jth TCE of the ith superlayer. The solid line divisions in the vectors and matrices denote divisions between superlayers and dotted line divisions denote divisions between TCEs. Note that $\mathbf{\Omega}(2)=\mathbf{\Omega}(2)^T$ and the base substrate is assumed to have an infinite thermal capacitance.

An alternative approach to constructing the governing equation in (5) is to treat each TCE as a building block and to build (5) through the addition of these building blocks. This assemblage is similar in nature to how the global mass and stiffness matrices are built from elemental matrices in FEM [53], although here the building blocks are different in nature from FEM. This approach generalizes the development of the governing equations in a way that can be applied to any generic part and corresponding TCN network, thus forming the foundation of our TCN model. For illustration, we demonstrate this approach for the part in Fig. 5.

Depending on the exact geometry, each TCE in the thermal circuit is categorized as a one of seven Types, as detailed in Section 3.2, and each Type corresponds to a specific building block matrix $\mathbf{\Omega}_{ij}$, given in Appendix B4. Consider, for example, the 2nd TCE of superlayer 1, which we will denote as [SL 1, TCE 2] for brevity. This TCE is considered to be TCE #2 and it is thermally connected to both the other TCE in superlayer 1 [SL 1, TCE 1] and also to the 1 st TCE in superlayer 2 [SL 2, TCE 1]. In general, we will speak of the building block as the TCE block at superlayer i with TCE number j and we will define our building blocks to describe intra-TCE heat flow as well as inter-TCE heat flow to the TCE below i,j, generically labeled as superlayer a and TCE number b. The building block matrix $\mathbf{\Omega}_{ij}$ for this TCE #2 is

$$\mathbf{\Omega}_{ij}=\begin{bmatrix}\mathbf{0} & \mathbf{0} & \mathbf{0} & \mathbf{0} & \mathbf{0} & \mathbf{0}\\ \mathbf{0} & -\Omega_{ij1} & 0 & \Omega_{ij1} & 0 & \mathbf{0}\\ \mathbf{0} & 0 & -\Omega_{ij3} & 0 & \Omega_{ij3} & \mathbf{0}\\ \mathbf{0} & \Omega_{ij1} & 0 & -\Omega_{ij1}-\Omega_{ij2} & \Omega_{ij2} & \mathbf{0}\\ \mathbf{0} & 0 & \Omega_{ij3} & \Omega_{ij2} & -\Omega_{ij2}-\Omega_{ij3} & \mathbf{0}\\ \mathbf{0} & \mathbf{0} & \mathbf{0} & \mathbf{0} & \mathbf{0} & \mathbf{0}\end{bmatrix}\begin{matrix}\longleftarrow ab1\\ \longleftarrow ab2\\ \longleftarrow ij1\\ \longleftarrow ij2\end{matrix}$$

$$\begin{matrix}\uparrow & \uparrow & \uparrow & \uparrow\\ ab1 & ab2 & ij1 & ij2\end{matrix} \tag{6}$$

where the labels with arrows denote the row and column of the entries. The other three TCEs in this example also fall into specific type classifications – #1 for [SL 2, TCE 1] and [SL 2, TCE 2] and #4 for [SL 1, TCE 1] – and have similarly constructed generic building block matrices (see Appendix B4). Each building block $\mathbf{\Omega}_{ij}$ is of size $\sum_{i=1}^{I}\sum_{j=1}^{J_i}K_{ij}\times\sum_{i=1}^{I}\sum_{j=1}^{J_i}K_{ij}$ with zero matrices $\mathbf{0}$ to fill out the matrix and appropriately align non-zero entries. Further, individual building blocks are symmetric: $\mathbf{\Omega}_{ij}=\mathbf{\Omega}_{ij}^T$.

This building block formulation enables a simple construction of the state equations in Eqn. (5) as

$$\mathbf{C}(i)\frac{d\mathbf{T}(i)}{dt}=\left(\sum_{a=1}^{i}\sum_{j=1}^{J_i}\mathbf{\Omega}_{aj}\right)\mathbf{T}(i)+\mathbf{P}(i). \tag{7}$$

$\mathbf{P}$(i) captures the heat flow from the radiant energy from the laser

$$\mathbf{P}(i)=[\mathbf{0}\quad\mathbf{P}_{iK_i}]^T. \tag{8}$$

Capacitance entries, C_{ijk}, conductance entries, $\Omega_{ijk,abc}$, and exogenous heat source entries, P_{ijk}, are determined by TV-level geometry and are detailed in Appendix B. This concludes the general assemblage of the system of ordinary differential equations to describe heat flow.

The following section will detail the assignment of TCE types, assignment of parameters of the matrices and vectors of Eq. (7), and the solution of Eq. (7). In short, the matrices and vectors in Eq. (7) are derived from the definition of different TCE Types and their relationship between other TCEs in the same superlayer as well as TCEs in adjacent superlayers. Additionally, Eq. (7) needs to be solved for a continually growing state equation as new superlayers are virtually added to our TCN.

3. Simulation description

3.1. An overview of the simulation modules

The flow chart in Fig. 6 shows an overview of the TCN program. The TCN program consists of three modules: an STL processor, a Metal PBF thermal model, and a mesh generator. The STL processor imports an STL files of the real part geometry, rotates the part geometry about x, y, and z axes, generates support structures as needed, and divides the part into superlayers, TCEs, and TVs, as demonstrated in Fig. 5. The Metal PBF model simulates the superlayer-by-superlayer process by solving Eq. (7) for each added superlayer. After the simulation is finished, the temperature from the thermal model is mapped to an FEM mesh by a mesh generator (Section 3.4).

3.2. Module I: STL processor

An STL file that defines the part is imported and then standard rotation and translation algorithms are applied to orient the part in the virtual build space as specified by user defined Euler angles or automatically generated Euler angles from an optimization routine (Appendix A1). The virtual part is then sliced along the z-direction into superlayers (Appendix A2) and then each superlayer is divided into TCEs and TVs. The TCEs are then categorized based on geometric relationships between slicing planes as described in the following subsection to build the thermal circuit.

3.2.1. TCE classification

The TCE structure leveraged in Section 2.5 labeled three types – #1, #2, and #4 – with minimal rationale for the type classification logic. This section provides the classification logic, which is dictated by the relative amount of horizontal heat transfer in the TCE and connections with adjacent TCE types. We define seven types of TCEs, TCE #1 through TCE #7. TCE #1 is the simplest network element representing purely vertical heat conduction. TCEs #2 and #3 reflect that there is an appreciable change in the projection of the area of one TCE on the adjacent TCE, leading the heat flow lines to either expand or constrict. TCEs #4 through #7 are modified version of TCEs #1 through #3, which will be discussed in detail below.

To determine whether or not there is an appreciable horizontal heat flow, a metric η is established that captures the normalized cross-sectional area change. First, the top or bottom surface of the TCE, whichever has a smaller area, is projected onto the geometric center of the other surface. The projected areas of the bottom and top surface of the jth TCE of the ith superlayer are denoted as S_{ij1} and S_{ij2}, respectively. The percentage increase of area from the bottom to the top surface is defined by

$$\eta = \frac{S_{ij2} - S_{ij1}}{S_{ij1}} \tag{9}$$

The metric η is provides an approximate correlate of the ratio of horizontal to vertical heat transfer (Appendix B1). If $|\eta|$ is less than critical value η_0, the horizontal heat transfer in the TCE is negligible and the assignment goes down the TCE #1 pathway (Fig. 7). Otherwise, the assignment goes down the TCE #2 or TCE #3 pathways, depending on whether the area is contracting or expanding, respectively. To determine the critical value η_0, heat transfer in truncated cones with different top surface areas were simulated in COMSOL Multiphysics®, and the overall horizontal and vertical heat fluxes were analyzed for each cone, as shown in Fig. 17 of Appendix B1. Based on this analysis, the critical value η_0 was set to be 20%. TCEs #4 through #7 are modifications from these TCE #1 through #3 assignments based on the TCE # of adjacent TCEs. Fig. 8 shows the seven types of TCEs.

After the types of TCEs are determined, the appropriate building block matrices $\mathbf{\Omega}_{ij}$ are assigned (Appendix B4), and the hierarchical governing equations for each superlayer are assembled, as shown in Section 2.5. The thermal capacitance and conductance parameters in the governing equations are automatically calculated from the physical properties of the metal and geometric information from the individual slices; details are included in Appendices B2 to B3. Fig. 7 demonstrates the automatic assignment of TCE type and the connections between superlayers and TCEs for a more complex part.

3.2.2. Support structures

Support structures are used to support the build process of overhanging features on a real part, and are represented by segments in this study. Similar to the virtual part, support structures are also modeled by leveraging the three levels of hierarchy as discussed in Section 2.3. The fundamental difference is that we do not consider horizontal heat transfer in support structures because the support structures typically have the geometry of a grid extruded in the z-direction, hence anisotropic conductance with the highest conductance in the z-direction. Support structures connecting the same TCE (or substrate) are lumped into a group. Each group of supports is then modeled as a serial connection of capacitance and conductance, serving as a heat path. As the support structure is porous, we assume that the effective thermal properties of the support material are scaled by the solid volume fraction, ϕ_s, of the support, $\lambda_s = \phi_s\lambda$ and $\tilde{c}_s = \phi_s\tilde{c}$ [54], where λ and $\tilde{c}$ are the bulk thermal properties as defined in Appendices B2 and B3.

3.2.3. Representative example

Section 2.5 provided a very simple example of a compound rectangular bar that contained three different TCE types. A more representative example of a complex part is shown in Fig. 9. Here we use a large discretization interval in the z-direction (8.3 mm) to demonstrate the correspondence between the part, the automatic assignment of TCE Type, interconnections between TCEs, superlayers, and support structures; a finer discretization interval is used in practice, as detailed in Section 4.

3.3. Module II: metal PBF thermal model

The Metal PBF thermal model simulates the virtual build cycle as successive superlayers are added to the model. A new superlayer is deposited onto the previously-built superlayers at the beginning of each build cycle. The laser heat source is uniformly applied to the top superlayer as a volumetric heat source until the average temperature of the top superlayer is above the liquidus temperature. Upon reaching the melting temperature, the laser heat source is set to 0, and all deposited superlayers cool down for a constant period of time, termed the effective inter-layer dwell time, t_{dwell}. As a superlayer has a volume that is approximately 30 times larger than a real layer, a thus will have a larger resistance and capacitance, it is not appropriate to use the real inter-layer dwell time from the machine parameters. To the best of the authors' knowledge, this artifact of increasing the z-direction discretization interval has not been studied. To estimate the effective inter-layer dwell time, we run a small simulation experiment at mid-height of the part using the real layer thickness and real inter-layer dwell time (50 μm and 10 s here) from the machine parameters. The effective inter-layer dwell time is adjusted to such that the thermal decay rates match. State Eqn. (1.7) is solved using the predictor-corrector method [55]. At the completion of the effective inter-dwell time, a new superlayer is

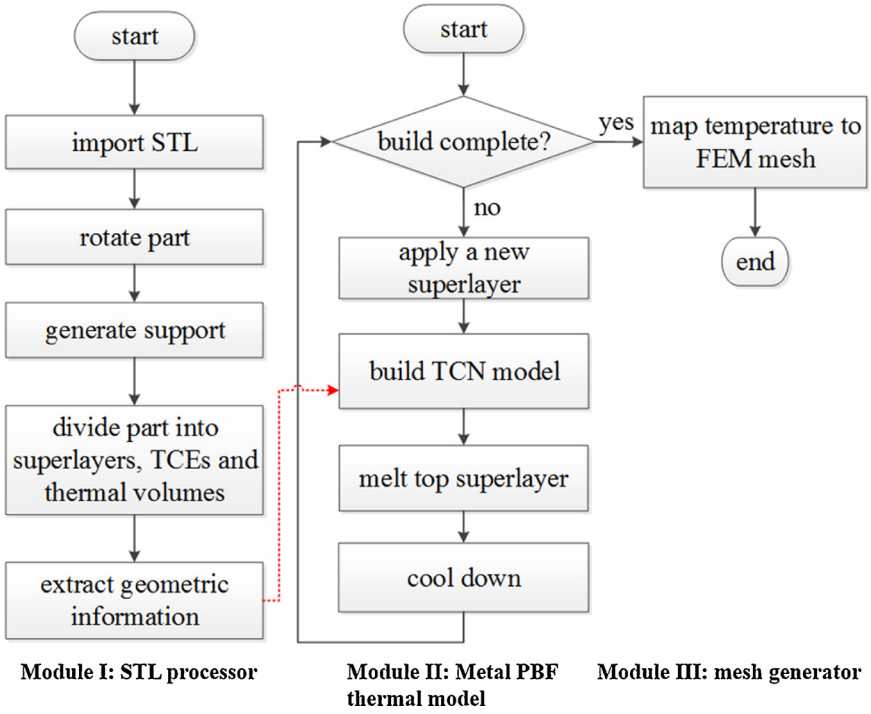

Fig. 6. An overview of the three modules of the TCN model. Module I: STL processor for rotating a part, generating support structures, and dividing the part into superlayers, TCEs, and TVs. Module II: a Metal PBF thermal model that simulates the temperature history during the superlayer-by-superlayer build cycle. Module III: a mesh generator for mapping temperatures from the thermal model to an FEM mesh.

added to the TCN and the initial conditions of the previously deposited superlayers are set to the final temperatures of the previous superlayer, $\mathbf{T}(i-1)|_{t=t_f}$, and the newly deposited superlayer is set to the ambient temperature: $\mathbf{T}(i)|_{t=0} = \left[\mathbf{T}(i-1)|_{t=t_f}^{T} \quad \mathbf{T}_0^T\right]^T$.

3.4. Module III: mesh generator

Ultimately, the dynamic temperature profiles from the thermal model must be mapped to an FEM mesh for FEM-based thermal distortion analysis (as outlined in the companion paper). The mapping is accomplished by using a Gauss kernel average smoother [56] (Appendix C). Briefly, the part and its supports are all represented by

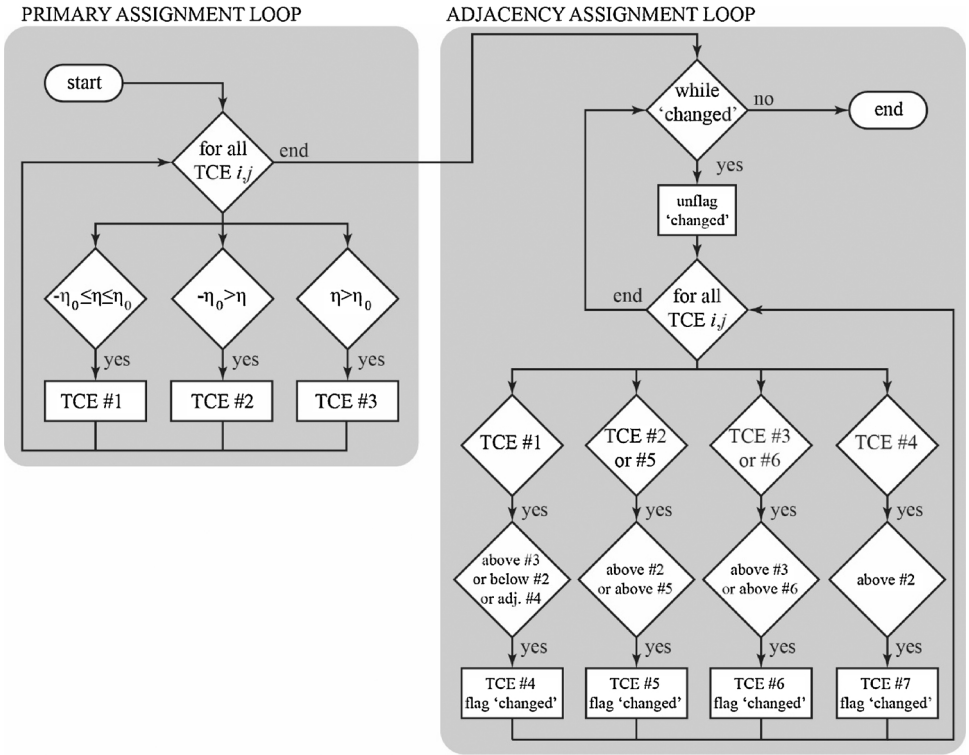

Fig. 7. Flow chart for TCE assignment. Primary assignment rules are applied based on metric η. Assignments are then modified by their adjacency to other TCEs to ensure that all thermal volumes are connected in the TCN; the adjacency loop runs continuously through the entire TCN until no further changes to TCE assignment are made.

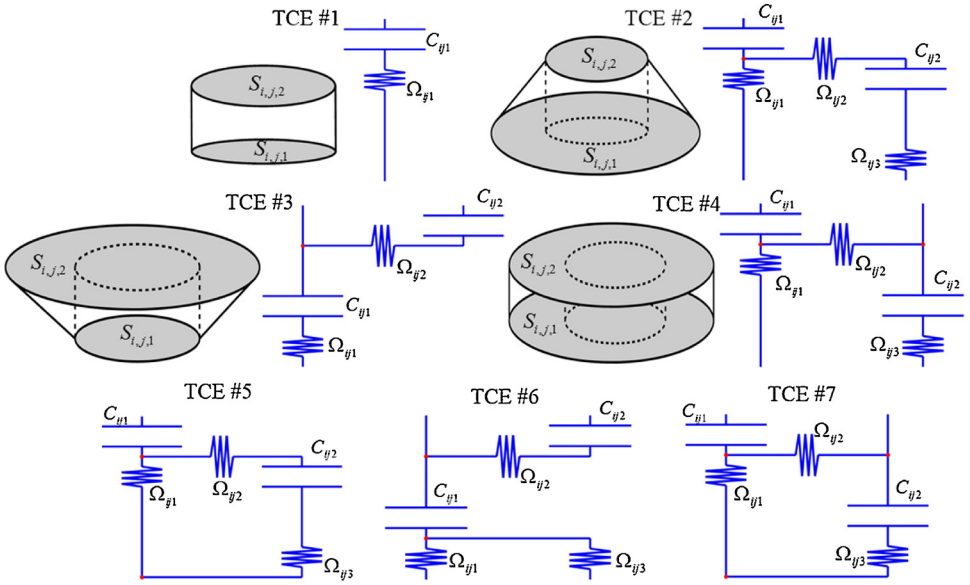

Fig. 8. Seven types of TCEs. TCE #1 with little cross-sectional area change from the bottom surface to top surface. TCE #2 with a significant decrease of cross-sectional area from the bottom surface to the top surface. TCE #3 with a significant increase of cross-sectional area from the bottom surface to the top surface. TCE #4 - #7 are modifications of #1 - #3 based the circuit connections required to connect adjacent TCEs.

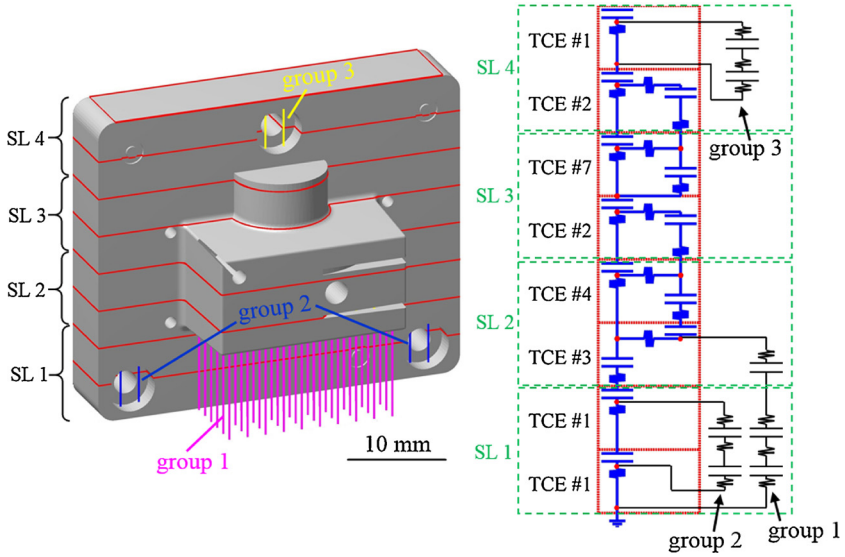

Fig. 9. Representative part and TCN. Part in the upright orientation divided into four superlayers with two TCEs per superlayer, and thermal circuit network (TCN) built by connecting a hierarchy of four superlayers, each with two TCEs and their associated thermal volumes.

rectangular cuboidal voxels, where each layer of voxels corresponds to a TV in the thermal model, and the temperature of the TV is mapped to the centers of the voxels. In a similar manner, the temperature of support TVs is also mapped to the centers of the support voxels. The temperatures at the nodes of the voxels are then estimated using a 3D Gauss kernel average smoother where the characteristic length scale of the kernel is the thermal diffusion length ($d_c = 2\sqrt{\alpha t_{dwell}}$, where α is the thermal diffusivity).

4. Simulation setup

A single complex part (Fig. 10) is used for a simulation study to compare the temperature history predictions between the proposed TCN model and a standard finite element method (FEM); our FEM simulation is similar in nature to the FEM analysis performed by [39]. We simulate two different build orientations – a flat orientation (Fig. 10a) and an upright orientation (Fig. 10b) – because they require different support structures, and thus allow us to demonstrate the generality of our TCN approach. The effective inter-layer dwell time used in this study is t_{dwell} = 25 s for both parts, with the inter-layer dwell time computed using the method introduced in Section 3.3. During the build process, the substrate is assumed to be maintained at a constant temperature 200 °C and the initial temperature of each thermal volume is 200 °C. The complete set of simulation parameters used for the TCN model and the FEM model are listed in Table 1. The thickness of a superlayer is slightly different between the flat (1.8 mm) and upright orientation (1.7 mm) because we force the analysis to use an integer number of superlayers; one superlayer is approximately 30 real build layers. There are four TCEs per superlayer and the Metal PBF processes of the flat and upright orientations are simulated by 10 and 20 build cycles, respectively. Both the TCN and FEM simulations were conducted on a conventional laptop (2.30 GHz processor and 8 GB memory).

Analogous to error metrics used in mesh convergence studies [53], we compared the predicted temperatures between the TCN and FEM by the relative error at each node at each time as

$$\mathbf{\Delta} = (\mathbf{T}_{TCN} - \mathbf{T}_{FEM}) \oslash \mathbf{T}_{FEM} \tag{10}$$

where ⊘ denotes element-wise division. We also report the Euclidean norm of the temperature of the voxels corresponding to a given

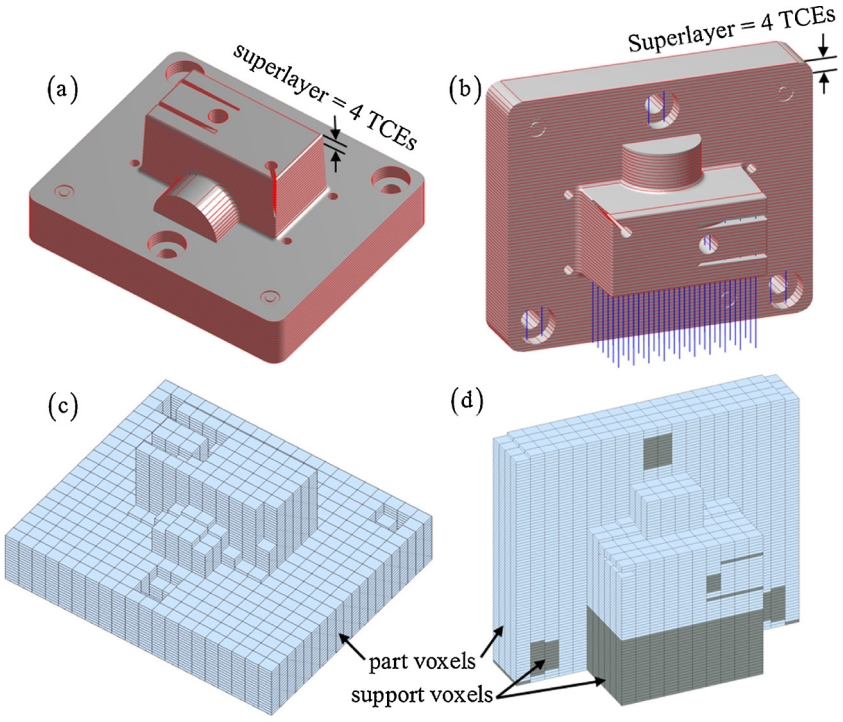

Fig. 10. Parts for FEM and TCN analysis. (a) and (b) A part in the flat and upright orientations for TCN analysis. (c) and (d) A part in the flat and upright orientations for FEM analysis.

superlayer as

$$|| \mathbf{T}(i) ||_2 \tag{11}$$

where i denotes voxels corresponding the ith superlayer and $||\bullet||_2$ is the L_2 norm.

The FEM model uses the same abstractions and assumptions in Section 2.2, but rather than solve a simplified thermal circuit, solves the full heat equation for the layer-by-layer build with a Fourier heat transfer constitutive equation [53]. The FEM model 1) imports a part from an STL file, 2) rotates the part to a user-defined orientation and 3) generates support structures underneath overhanging surfaces. Both the part and supports are then meshed into voxels (Fig. 10(c) and (d)) [57–59]. Each voxel is categorized as a *part voxel* or a *support voxel* based on the location of the voxel center. Although voxels cannot accurately represent curved surfaces, the advantages of voxel representation are readily applicable to Metal PBF: 1) The addition of new virtual layers is simply the addition of new a superlayer or superlayers of voxels; 2) The support structures is easily denoted by a difference in material properties; 3) The voxels can be directly used as rectangular cuboidal elements for FEM analysis. We discretized the flat orientation into $20 \times 20 \times 40$ voxels and the upright orientation into $20 \times 10 \times 80$ voxels, respectively.

Table 1
TCN and FEM parameters.

Parameters	Flat part	Upright part
Number of superlayers I	10	20
TCEs per superlayer J_i	4	4
Thickness of a superlayer	1.8 mm	1.7 mm
Effective inter-layer dwell time t_{dwell}	25 s	25 s
Substrate temperature T_0	200 °C	200 °C
Material	Ti-6Al-4V	Ti-6Al-4V
Volume fraction of support structures	42%	42%
Volumetric laser power density	3×10^{12} W/m^3	3×10^{12} W/m^3

5. Simulation results

Figs. 11 and 12 show the evolution of the temperature profile during the build of the part in the flat and upright build orientations, respectively, as predicted by our TCN model. In comparing the temperature profiles in Figs. 11 and 12, it is clear that there is a large temperature gradient concentration located at the top superlayers of the flat orientation while the temperature gradient in the upright orientation decreases gradually from the top to bottom layers. This is because the thermal conductance in the vertical part is smaller due to smaller cross-sectional area. Furthermore, the temperature profiles in superlayers 7 through 20 in the upright orientation show that the extruded boss maintains an elevated temperature compared to the main body, as it loses much of its thermal energy through the support structure, which has a lower effective thermal conductance. If we conduct the analysis without the support structure, there is even less thermal conduction from the boss and the temperature is about 400 °C higher on average, which often leads to dross formation and hence a rough surface.

The relative error, $\boldsymbol{\Delta}$, between the TCN and FEM analyses in the flat orientation is generally less than 5% for the initial four superlayers, and increases to approximately 15% at the top layer when the fifth superlayer is built (Fig. 13). From the sixth to the tenth superlayer, the relative error is generally less than 15% with relatively larger error at the four corners of the part. The relative error in the upright orientation is generally less than 5% throughout the entire build process, although the error approaches 15% near the boss and near the two holes near the base (Fig. 14).

Fig. 15(a) and (b) show the time evolution of the average temperature in each superlayer, $|| \mathbf{T}(i) ||_2$, for the flat and upright orientations. At the beginning of every virtual build cycle, the top-most superlayer is heated up to the liquidus temperature of the material followed by the termination of the laser heat source, $\mathbf{P}(i) = 0$. This virtual paradigm can be seen in the temperature cycling of every superlayer as the heat is dissipated from the top-most superlayer during each virtual build cycle. Due to latent heat of melting and solidification, there is a plateau region between the liquidus and solidus temperature

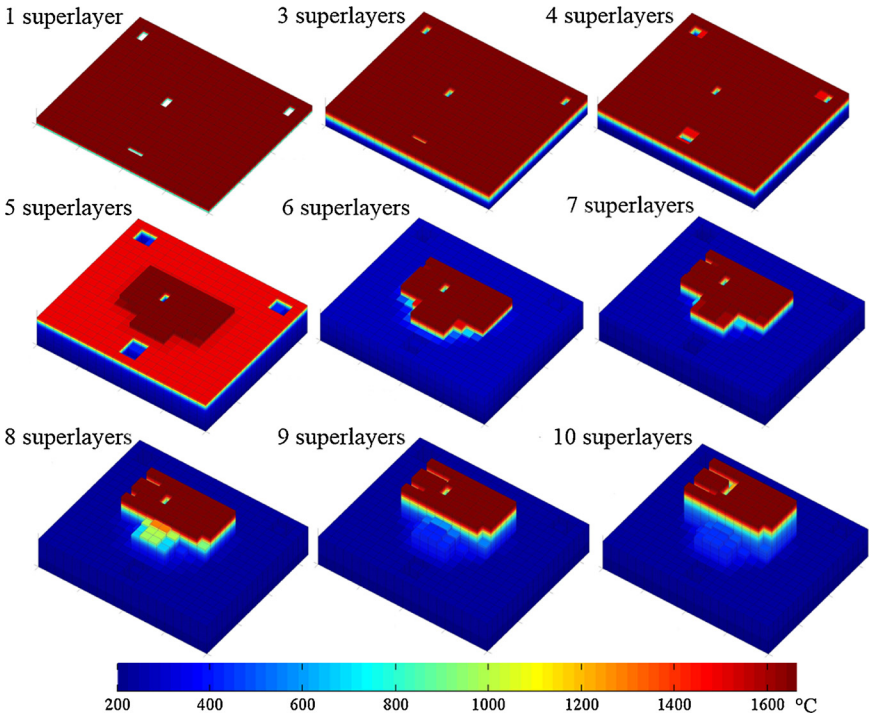

Fig. 11. Part build and temperature profile evolution in the flat orientation as predicted by the TCN. The time point shown is the moment immediately after the top superlayer is fully solidified.

line for each thermal decay curve. The time constant for the thermal decay of the top superlayer increases as more superlayers are deposited because both the thermal capacitance and resistance of the entire part increases. Finally, after all superlayers are deposited, the part cools down to room temperature.

Qualitatively, $||\mathbf{T}(i)||_2$ curves for the TCN and FEM match well for both build orientations. We observe the greatest deviation between the two models during the cooling period (dwell time) after the top-most superlayer reaches the solidus temperature (Fig. 15(a)); these layers have the strongest thermal gradient. The TCN generally underpredicts the $||\mathbf{T}(i)||_2$ values compared to the more accurate FEM, but the difference in $||\mathbf{T}(i)||_2$ does not exceed 10% for either build orientation.

The TCN and the FEM simulations are compared in Table 2. The computational time of the thermal FEM model is 14 h 10 min for the flat orientation and 41 h 15 min for the upright orientation. In contrast, the computational time of the TCN model is 2 min for the flat orientation and 18 min 43 s for the upright orientation. The TCN is more than two orders of magnitude faster than the FEM approach, but, as noted above,

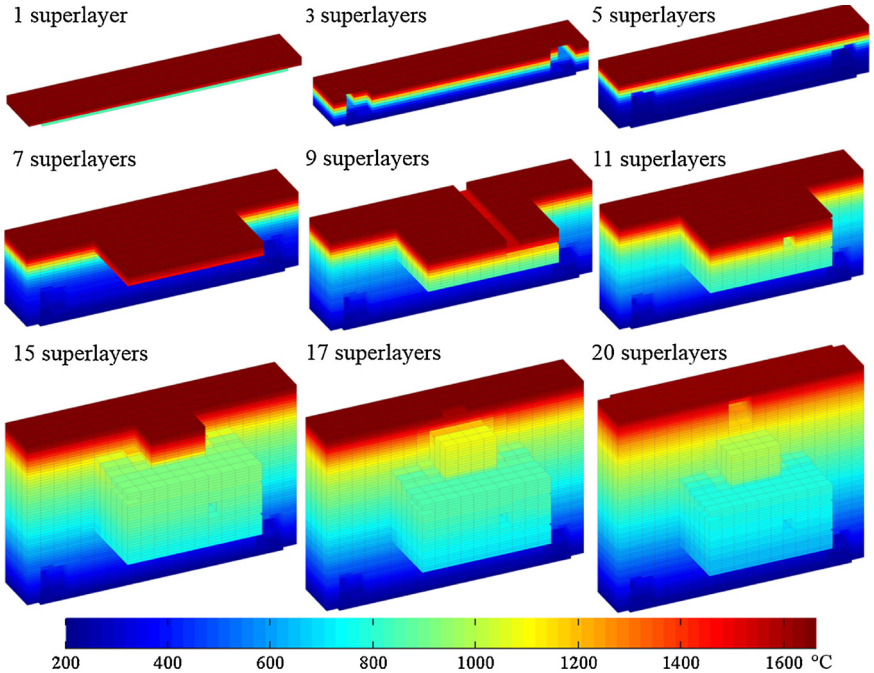

Fig. 12. Part build and temperature profile evolution in the upright orientation as predicted by the TCN. The time point shown is the moment immediately after the top superlayer is fully solidified.

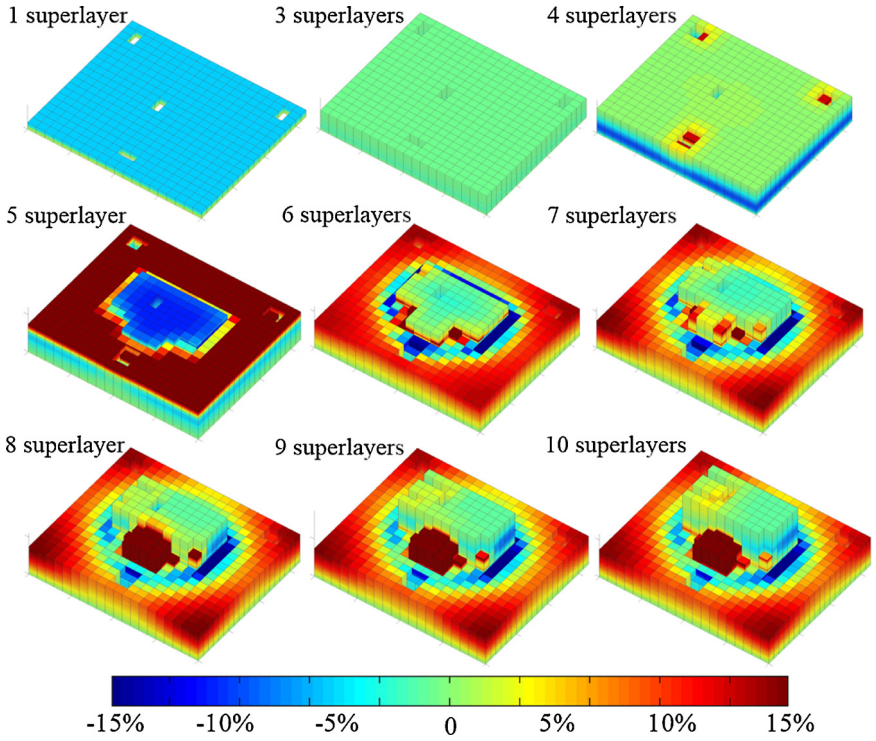

Fig. 13. Relative error **Δ** between TCN and FEM temperature predictions for the flat orientation. The time point shown is the moment immediately after the top superlayer is fully solidified.

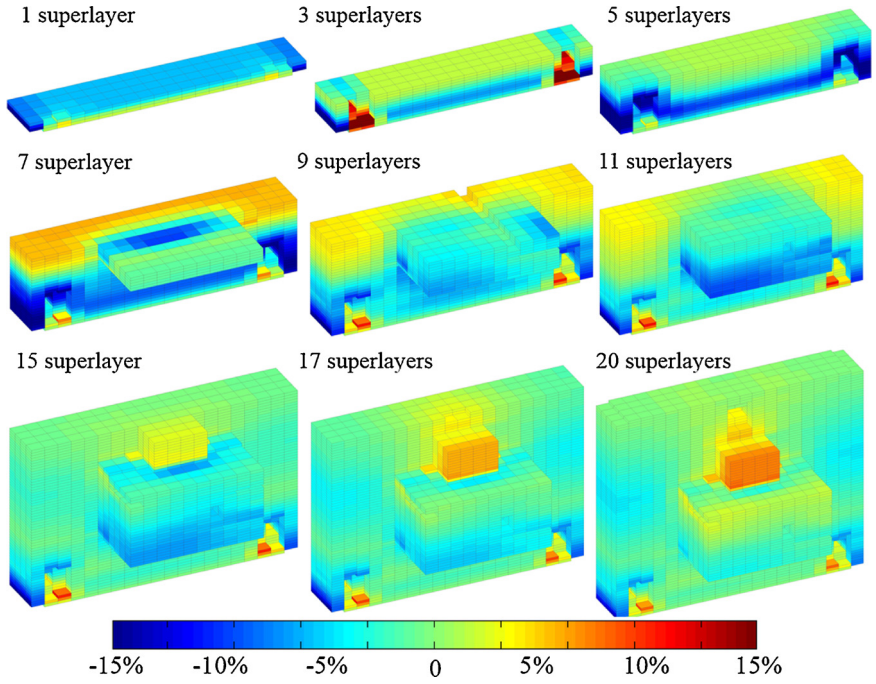

Fig. 14. Relative error **Δ** between TCN and FEM temperature predictions for the upright orientation. The time point shown is the moment immediately after the top superlayer is fully solidified.

at most only results in a 15% difference in the temperature profile of the part.

6. Summary and future studies

Proper Metal PBF design is not intuitive and only well-understood by well-trained Metal PBF technicians and researchers. For Metal PBF to be used *en masse*, we will need automatic algorithms to automatically design optimal build orientations and support structures. The objective function in these automatic algorithms must be computed efficiently to converge to an optimal design on the time frame of one day on a conventional computer. This manuscript demonstrates an alternative method to FEM to predict the temperature profile using a simplified thermal circuit approach; we demonstrate that there is a significant computational advantage to our TCN approach over more accurate, but intensive, numerical schemes such as FEM. In general, the TCN model

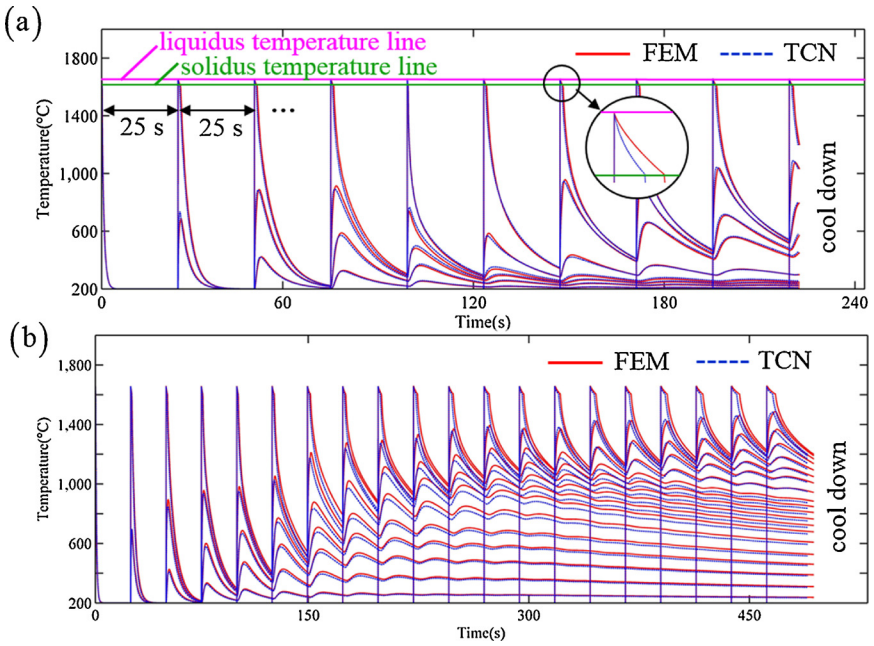

Fig. 15. Average temperature of each superlayer predicted by TCN and FEM. (a) flat orientation (b) upright orientation.

Table 2
Comparison of TCN and thermal FEM simulations.

Model	Number of superlayers	TCEs per superlayer	Computational time	Relative error
TCN for flat orientation	10	4	2 min	< 15%
TCN for upright orientation	20	4	18 min 43 s	< 15%
FEM for flat orientation	10	4	14 h 10 min	/
FEM for upright orientation	20	4	41 h 15 min	/

can predict the temperature history with more than two orders of magnitude faster computational speed while sacrificing less than 15% accuracy. An error of 15% is within the range of the prediction errors from the current state-of-the-art computational packages for Metal PBF [34,60–62]. Lastly, as the ultimate aim of this fast algorithm is for integration into design optimization algorithms, once an algorithm has converged to an optimal design, a more thorough computational FEM model could be applied to verify the results or optimize over a reduced design range after eliminating poor designs.

Future work will directly use the TCN given in this manuscript and the quasi-static thermomechanical model in the companion manuscript in an optimization algorithm to automatically converge to an optimal orientation with respect to the part thermal distortion. There are many potential future directions for the TCN detailed here. Additionally, our current set of seven TCE types are somewhat limited in that they do not accommodate branched parts, which will have more than two TVs per TCE. There is a wealth of literature in graph theoretic [63] and geometric modeling that can be integrated into our general TCN framework presented here to accommodate branched, complex part architectures.

Acknowledgements and Disclaimer

This material is based on research sponsored by Air Force Research Laboratory under agreement number FA8650-12-2-7230. The U.S. Government is authorized to reproduce and distribute reprints for Governmental purposes notwithstanding any copyright notation thereon. The views and conclusions contained herein are those of the authors and should not be interpreted as necessarily representing the official policies or endorsements, either expressed or implied, of Air Force Research Laboratory or the U.S. Government.

Appendix A. STL Processor

A1 Part orientation and support generation

An STL file describes the surface of a part by unit normal and vertices of triangles. The STL processor imports STL files by using an STL reader written by Esmonde-White [64]. Then the STL processor rotates the parts about the x, y and z axes to a user-defined orientation. Once the part is placed in a given orientation, the STL processor generates support structures under *critical surfaces,* which are defined as any triangle with an inclination angle less than 35° relative to the horizontal [21]. First, the part is projected onto the xy plane, and the projection is bounded by a rectangle with edges parallel to the x and y axes. The rectangle is discretized into a user-defined number of grids. From the center of each grid, a virtual ray is extended in the positive z direction from the grid and intersects with the part surface. The intersecting points, if any, break the ray into several segments. If a segment is outside of the part, and the upper end of the segment is on a *critical surface*, then the segment is a support structure. Both external and internal support structures can be generated with this algorithm.

A2 Part Slicing

Another function of the STL processor is to divide a part into superlayers, TCEs and TVs by using the slicing algorithm proposed by Choi and

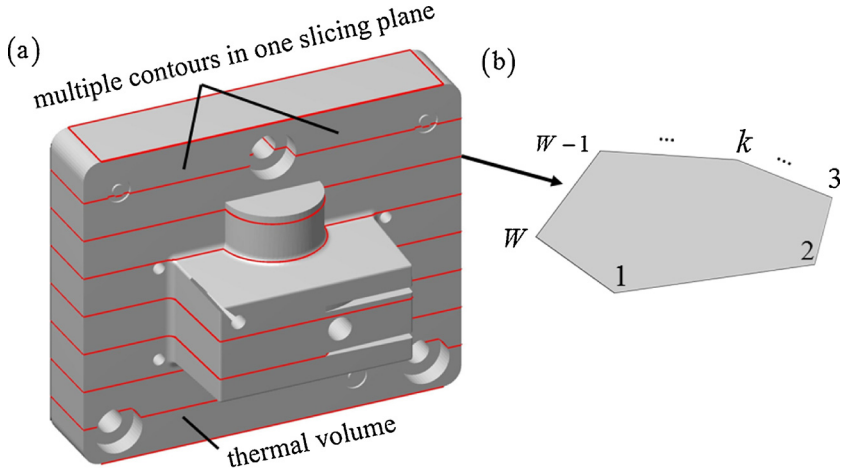

Fig. 16. Division of a part into individual TCEs. (a) A part divided into eight TCEs, and (b) an example of a polygon contour.

Kwok [65], as shown in Fig. 16(a). The TCEs are separated by polygon contours as shown in Fig. 16(b). Taking the jth TCE of the *i*th superlayer for instance, the cross-sectional area formed by the contour at the bottom surface of the TCE can be calculated with [66]

$$\overline{S}_{ij1} = \frac{1}{2}\left|\sum_{v=1}^{W-1}(x_v y_{v+1} - y_v x_{v+1}) + (x_N y_1 - y_N x_1)\right| \tag{12}$$

where W is the total number of vertices in the contour and x_v and y_v are the x and y coordinates of the vth vertex (Fig. 16(b)). Multiple contours may occur in one slicing plane (Fig. 16(a)) and the relation between these contours can be hierarchical. In such cases, a hierarchy-sorting algorithm [65] is used to obtain the cross-sectional area.

Appendix B. Metal PBF parameters and TCE state equations

B1 Critical value of η_0

To determine the critical value η_0 for the criteria in Eq. (9), the heat transfer in truncated cones with different top surface areas was simulated using COMSOL Multiphysics®. The thickness of the truncated cones was set to be 2 mm and the diameter of the bottom circle was set to be 20 mm. The diameter of the top circle was varied so that η = 10%, 20%, 40%, 60%, 80%, and 100% respectively. Non-dimensionalized temperatures at the top and bottom surfaces are set to be 1 and 0, and the steady-state heat flux is analyzed. The ratios of overall horizontal heat transfer to vertical heat transfer are 3.5%, 4.6%, 7.4%, 12.5%, 12.6% and 12.7% for each case, as shown in Fig. 17. As the horizontal heat transfer relative to vertical is less than 5% at η = 20%, the critical value η_0 is chosen to be 20% in this study.

B2 Thermal capacitance

The capacitance parameters in the governing equations are determined by physical properties and geometric information from the STL processor. Taking TCE #2 for instance, the thermal capacitance C_{ij1} and C_{ij2} are estimated as

$$\begin{aligned} C_{ij1} &= \rho L \overline{S}_{ij2} \tilde{c}_p \\ C_{ij2} &= \tfrac{1}{2}\rho L(\overline{S}_{ij1} - \overline{S}_{ij2})\tilde{c}_p \end{aligned} \tag{13}$$

where ρ is density, L is the thickness of the jth TCE of the *i*th superlayer, $\overline{S}_{ij1}$ and $\overline{S}_{ij2}$ are cross-sectional areas at the bottom and top surfaces of the TCE (see Eq. (1.12)), and $\tilde{c}_p$ is effective thermal capacity defined as [67]

$$\tilde{c}_p = \begin{cases} c_p & T_{ij1}\,(\text{or}T_{ij2}) \geq T_l \\ c_p + \frac{h_{sl}}{T_l - T_s} & T_s < T_{ij1}\,(\text{or}T_{ij2}) < T_l \\ c_p & T_{ij1}\,(\text{or}T_{ij2}) \leq T_s \end{cases} \tag{14}$$

where c_p is thermal capacity of a given material, h_{sl} is the melting/solidification latent heat, and T_l and T_s are liquidus and solidus temperature of material. Equation (1.14) models the increase of heat capacity due to latent heat during the melting and solidification process.

B3 Thermal Conductance

The thermal conductance parameters between TVs are dependent on the geometry of the thermal volumes and the material properties. Depending on the configuration of the TVs, the conductance can describe either vertical or horizontal heat transfer.

(15) Vertical thermal conductance

Taking TCE #2 for instance, the vertical thermal conductance Ω_{ij1} and Ω_{ij3} are estimated as

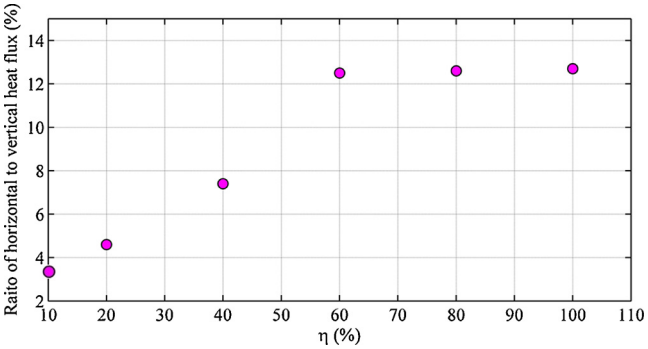

Fig. 17. Study of η versus ratio of horizontal and vertical heat flux. The ratios of overall horizontal heat flux to vertical heat flux in circular truncated cones with cross-sectional area increase from bottom to top to be 10%, 20%, 40%, 60%, 80% and 100%.

$$\Omega_{ij1} = \frac{\lambda \bar{S}_{ij2}}{L}$$
$$\Omega_{ij3} = \frac{\lambda (\bar{S}_{ij1} - \bar{S}_{ij2})}{L} \tag{15}$$

where λ is thermal conductivity, L is the thickness of the jth TCE of the ith superlayer, $\bar{S}_{ij1}$ and $\bar{S}_{ij2}$ are cross-sectional areas at the bottom and top surfaces of the TCE.

(16) Horizontal thermal conductance

Horizontal thermal conductance Ω_{ij2} is required for modeling TCEs #2 to #7. Here, a ray-shooting method is proposed to estimate Ω_{ij2}. Taking TCE #2 for instance, Fig. 18(a) and (b) show the projection of $\bar{S}_{ij2}$ onto $\bar{S}_{ij1}$. Note part of $\bar{S}_{ij2}$ can be outside of $\bar{S}_{ij1}$ as shown in Fig. 18(b). First, the geometric center O of $\bar{S}_{ij2}$ is located. Starting from O, rays are uniformly shot outward and the mth ray intersects $\bar{S}_{ij1}$ at M_m. No rays shoot outside of $\bar{S}_{ij1}$. Assuming each ray represents a thermal conductance connecting $\bar{S}_{ij1}$ and $\bar{S}_{ij2}$, the horizontal thermal conductance Ω_{ij2} is the sum of these conductance in parallel. If the thermal conductance of the mth ray is estimated as

$$\Omega_{ij2} = 1/\frac{\lambda L \Delta l_m}{\| \overrightarrow{OM_m} \|/4} \tag{16}$$

where λ is thermal conductivity, $\| \overrightarrow{OM_m} \|/4$ is estimated to be the length of the conductance, $L\Delta l_m$ is the cross-sectional area of the conductance, then the total horizontal thermal conductance is estimated to be

$$\Omega_{ij2} = 1/\sum_{m=1}^{M_r} \frac{4\lambda L \Delta l_m}{\| \overrightarrow{OM_m} \|} \tag{17}$$

where M_r is the total number of rays and $M_r = 20$ is used in this paper.

B4 TCE building blocks

This section details the conductance building block for each TCE type. For each, it is assumed that the building block corresponds to the ith superlayer and jth TCE and is immediately above the ath superlayer and bth TCE.

TCE Type 1.

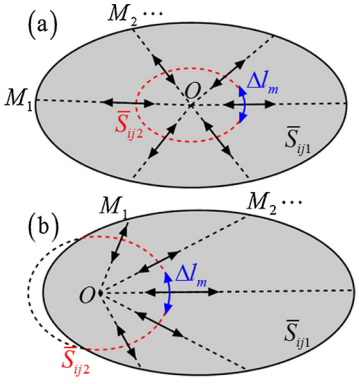

Fig. 18. Ray-shooting method for estimating horizontal thermal conductance. Projection of $\bar{S}_{ij2}$ to $\bar{S}_{ij1}$ where the projection (a) within and (b) outside $\bar{S}_{ij1}$.

$$\boldsymbol{\Omega}_{ij} = \begin{bmatrix} \mathbf{0} & \mathbf{0} & \mathbf{0} & \mathbf{0} \\ \mathbf{0} & -\Omega_{ij1} & \Omega_{ij1} & \mathbf{0} \\ \mathbf{0} & \Omega_{ij1} & -\Omega_{ij1} & \mathbf{0} \\ \mathbf{0} & \mathbf{0} & \mathbf{0} & \mathbf{0} \end{bmatrix} \begin{matrix} \\ \longleftarrow ab1 \\ \longleftarrow ij1 \\ \\ \end{matrix} \\ \begin{matrix} \uparrow & \uparrow \\ ab1 & ij1 \end{matrix} \tag{18}$$

TCE Type 2.

$$\boldsymbol{\Omega}_{ij} = \begin{bmatrix} \mathbf{0} & \mathbf{0} & \mathbf{0} & \mathbf{0} & \mathbf{0} & \mathbf{0} \\ \mathbf{0} & -\Omega_{ij1} & 0 & \Omega_{ij1} & 0 & \mathbf{0} \\ \mathbf{0} & 0 & -\Omega_{ij3} & 0 & \Omega_{ij3} & \mathbf{0} \\ \mathbf{0} & \Omega_{ij1} & 0 & -\Omega_{ij1} - \Omega_{ij2} & \Omega_{ij2} & \mathbf{0} \\ \mathbf{0} & 0 & \Omega_{ij3} & \Omega_{ij2} & -\Omega_{ij2} - \Omega_{ij3} & \mathbf{0} \\ \mathbf{0} & \mathbf{0} & \mathbf{0} & \mathbf{0} & \mathbf{0} & \mathbf{0} \end{bmatrix} \begin{matrix} \\ \longleftarrow ab1 \\ \longleftarrow ab2 \\ \longleftarrow ij1 \\ \longleftarrow ij2 \\ \\ \end{matrix} \\ \begin{matrix} \uparrow & \uparrow & \uparrow & \uparrow \\ ab1 & ab2 & ij1 & ij2 \end{matrix} \tag{19}$$

TCE Type 3.

$$\boldsymbol{\Omega}_{ij} = \begin{bmatrix} \mathbf{0} & \mathbf{0} & \mathbf{0} & \mathbf{0} & \mathbf{0} \\ \mathbf{0} & -\Omega_{ij1} & \Omega_{ij1} & 0 & \mathbf{0} \\ \mathbf{0} & \Omega_{ij1} & -\Omega_{ij1} - \Omega_{ij2} & \Omega_{ij2} & \mathbf{0} \\ \mathbf{0} & 0 & \Omega_{ij2} & -\Omega_{ij2} & \mathbf{0} \\ \mathbf{0} & \mathbf{0} & \mathbf{0} & \mathbf{0} & \mathbf{0} \end{bmatrix} \begin{matrix} \\ \longleftarrow ab1 \\ \longleftarrow ij1 \\ \longleftarrow ij2 \\ \\ \end{matrix} \\ \begin{matrix} \uparrow & \uparrow & \uparrow \\ ab1 & ij1 & ij2 \end{matrix} \tag{20}$$

TCE Type 4.

$$\boldsymbol{\Omega}_{ij} = \begin{bmatrix} \mathbf{0} & \mathbf{0} & \mathbf{0} & \mathbf{0} & \mathbf{0} & \mathbf{0} \\ \mathbf{0} & -\Omega_{ij1} & 0 & \Omega_{ij1} & 0 & \mathbf{0} \\ \mathbf{0} & 0 & -\Omega_{ij3} & 0 & \Omega_{ij3} & \mathbf{0} \\ \mathbf{0} & \Omega_{ij1} & 0 & -\Omega_{ij1} - \Omega_{ij2} & \Omega_{ij2} & \mathbf{0} \\ \mathbf{0} & 0 & \Omega_{ij3} & \Omega_{ij2} & -\Omega_{ij2} - \Omega_{ij3} & \mathbf{0} \\ \mathbf{0} & \mathbf{0} & \mathbf{0} & \mathbf{0} & \mathbf{0} & \mathbf{0} \end{bmatrix} \begin{matrix} \\ \longleftarrow ab1 \\ \longleftarrow ab2 \\ \longleftarrow ij1 \\ \longleftarrow ij2 \\ \\ \end{matrix} \\ \begin{matrix} \uparrow & \uparrow & \uparrow & \uparrow \\ ab1 & ab2 & ij1 & ij2 \end{matrix} \tag{21}$$

TCE Type 5.

$$\boldsymbol{\Omega}_{ij} = \begin{bmatrix} \mathbf{0} & \mathbf{0} & \mathbf{0} & \mathbf{0} & \mathbf{0} \\ \mathbf{0} & -\Omega_{ij1} - \Omega_{ij3} & \Omega_{ij1} & \Omega_{ij3} & \mathbf{0} \\ \mathbf{0} & \Omega_{ij1} & -\Omega_{ij1} - \Omega_{ij2} & \Omega_{ij2} & \mathbf{0} \\ \mathbf{0} & \Omega_{ij3} & \Omega_{ij2} & -\Omega_{ij2} - \Omega_{ij3} & \mathbf{0} \\ \mathbf{0} & \mathbf{0} & \mathbf{0} & \mathbf{0} & \mathbf{0} \end{bmatrix} \begin{matrix} \\ \longleftarrow ab1 \\ \longleftarrow ij1 \\ \longleftarrow ij2 \\ \\ \end{matrix} \\ \begin{matrix} \uparrow & \uparrow & \uparrow \\ ab1 & ij1 & ij2 \end{matrix} \tag{22}$$

TCE Type 6.

$$\boldsymbol{\Omega}_{ij} = \begin{bmatrix} \mathbf{0} & \mathbf{0} & \mathbf{0} & \mathbf{0} & \mathbf{0} & \mathbf{0} \\ \mathbf{0} & -\Omega_{ij1} & 0 & \Omega_{ij1} & 0 & \mathbf{0} \\ \mathbf{0} & 0 & -\Omega_{ij3} & \Omega_{ij3} & 0 & \mathbf{0} \\ \mathbf{0} & \Omega_{ij1} & \Omega_{ij3} & -\Omega_{ij1} - \Omega_{ij2} & \Omega_{ij2} & \mathbf{0} \\ \mathbf{0} & 0 & & \Omega_{ij2} & -\Omega_{ij2} & \mathbf{0} \\ \mathbf{0} & \mathbf{0} & \mathbf{0} & \mathbf{0} & \mathbf{0} & \mathbf{0} \end{bmatrix} \begin{matrix} \\ \longleftarrow ab1 \\ \longleftarrow ab2 \\ \longleftarrow ij1 \\ \longleftarrow ij2 \\ \\ \end{matrix} \\ \begin{matrix} \uparrow & \uparrow & \uparrow & \uparrow \\ ab1 & ab2 & ij1 & ij2 \end{matrix} \tag{23}$$

TCE Type 7.

$$\boldsymbol{\Omega}_{ij} = \begin{bmatrix} \mathbf{0} & \mathbf{0} & \mathbf{0} & \mathbf{0} & \mathbf{0} \\ \mathbf{0} & -\Omega_{ij1} - \Omega_{ij3} & \Omega_{ij1} & \Omega_{ij3} & \mathbf{0} \\ \mathbf{0} & \Omega_{ij1} & -\Omega_{ij1} - \Omega_{ij2} & \Omega_{ij2} & \mathbf{0} \\ \mathbf{0} & \Omega_{ij3} & \Omega_{ij2} & -\Omega_{ij2} - \Omega_{ij3} & \mathbf{0} \\ \mathbf{0} & \mathbf{0} & \mathbf{0} & \mathbf{0} & \mathbf{0} \end{bmatrix} \begin{matrix} \longleftarrow ab1 \\ \longleftarrow ij1 \\ \longleftarrow ij2 \\ \\ \\ \end{matrix}$$
$$\begin{matrix} \uparrow & \uparrow & \uparrow \\ ab1 & ij1 & ij2 \end{matrix} \tag{24}$$

Appendix C. Mesh Generator

The mesh generator converts the irregularly discretized TCN TV nodes into a rectangular cuboidal voxel mesh for integration into an FEM solver.

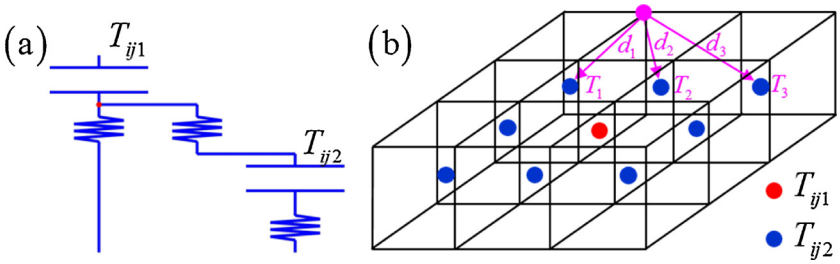

Fig. 19. Mesh generation schematic. (a) Temperatures of two thermal volumes of the *j*th TCE of the *i*th superlayer from the TCN model. (b) Mapping the two temperatures from TCN model to an FEM mesh. The purple node denotes the current node of interest, *T*, and the red and blue nodes denote temperatures directly mapped from the geometric overlap of the TV geometry and the rectangular cuboidal voxel mesh (For interpretation of the references to colour in this figure legend, the reader is referred to the web version of this article).

The TCN is first mapped to rectangular cuboidal voxel mesh by assigning the temperatures of voxel centers that overlap with a given TV the temperature of the corresponding TV. For instance, assuming temperatures of the thermal volumes at the *j*th TCE of the *i*th superlayer are T_{ij1} and T_{ij2}, as shown in Fig. 19(a), these two temperatures are assigned to the centers of the mesh voxels based on the location of the thermal volumes as shown in Fig. 19(b). Similarly, the temperatures of the support structures from TCN are assigned to the centers of the support voxels.

After the centers of each voxel have been assigned a temperature, the temperatures of all mesh nodes filtered by using

$$T = \sum_{n=1}^{N} D_n T_n \Big/ \sum_{n=1}^{N} D_n \tag{25}$$

where D_n is the 3-D Gauss kernel average smoother defined as

$$D_n = \exp\left(-\frac{d_n^2}{d_c^2}\right) \tag{26}$$

d_n is the distance between the node and the *n*th voxel center as shown in Fig. 19(b) and d_c is the characteristic length of thermal conduction which is defined as [68]

$$d_c = 2\sqrt{\alpha t_{dwell}} \tag{27}$$

α is thermal diffusivity and t_{dwell} is the inter-layer dwell time as defined in Section 3.3. T_n is the temperature at the *n*th voxel center, and temperature at the node is the average temperature at *N* voxel centers nearest to the node.

References

[1] H. Peng, M. Ghasri-Khouzani, S. Gong, R. Attardo, P. Ostiguy, B. Aboud Gatrell, J. Budzinski, C. Tomonto, J. Neidig, M.R. Shankar, R. Billo, D.B. Go, D.J. Hoelzle, Fast prediction of thermal distortion in metal powder bed fusion additive manufacturing; Part 2: a quasi-static thermo-mechanical model, Submitt. Addit. Manuf. (2017).

[2] Standard Terminology for Additive Manufacturing Technologies, (Withdrawn 2015), (2015).

[3] W. Frazier, Metal additive manufacturing: a review, J. Mater. Eng. Perform. 23 (2014) 1917–1928, http://dx.doi.org/10.1007/s11665-014-0958-z.

[4] D.D. Gu, W. Meiners, K. Wissenbach, R. Poprawe, Laser additive manufacturing of metallic components: materials, processes and mechanisms, Int. Mater. Rev. 57 (2012) 133–164, http://dx.doi.org/10.1179/1743280411y.0000000014.

[5] I. Gibson, D.W. Rosen, B. Stucker, Additive Manufacturing Technologies: Rapid Prototyping to Direct Digital Manufacturing, Springer, US, 2009.

[6] K.P. Karunakaran, A. Bernard, S. Suryakumar, L. Dembinski, G. Taillandier, Rapid manufacturing of metallic objects, Rapid Prototyp. J. 18 (2012) 264–280, http://dx.doi.org/10.1108/13552541211231644.

[7] L.E. Murr, S.M. Gaytan, D.A. Ramirez, E. Martinez, J. Hernandez, K.N. Amato, P.W. Shindo, F.R. Medina, R.B. Wicker, Metal fabrication by additive manufacturing using laser and electron beam melting technologies, J. Mater. Sci. Technol. 28 (2012) 1–14, http://dx.doi.org/10.1016/s1005-0302(12)60016-4.

[8] B. Vayre, F. Vignat, F. Villeneuve, Metallic additive manufacturing: state-of-the-art review and prospects, Mech. Ind. 13 (2012) 89–96, http://dx.doi.org/10.1051/meca/2012003.

[9] X. Gong, T. Anderson, K. Chou, Review on powder-based electron beam additive manufacturing technology, Manuf. Rev. 1 (2014) 2, http://dx.doi.org/10.1051/mfreview/2014001.

[10] H.M. Chae, A numerical and experimental study for residual stress evolution in low alloy steel during laser aided additive manufacturing process, Ph.D. Thesis in Mechanical Engineering, University of Michigan, 2013.

[11] W. King, A.T. Anderson, R.M. Ferencz, N.E. Hodge, C. Kamath, S.A. Khairallah, Overview of modelling and simulation of metal powder bed fusion process at Lawrence livermore national laboratory, Mater. Sci. Technol. 31 (2015) 957–968, http://dx.doi.org/10.1179/1743284714Y.0000000728.

[12] N.P. Lavery, S.G.R. Brown, J. Sienz, J. Cherry, F. Belblidia, A review of computational modelling of additive layer manufacturing-multi-scale and multi-physics, Int. Conf. Sustain. Des. Manuf. Cardiff, Wales, UK, 2014.

[13] M. Megahed, H.-W. Mindt, N. N'Dri, H. Duan, O. Desmaison, Metal additive-manufacturing process and residual stress modeling, Integrating Mater. Manuf. Innov. 5 (2016) 1–33, http://dx.doi.org/10.1186/s40192-016-0047-2.

[14] K. Zeng, D. Pal, H.J. Gong, N. Patil, B. Stucker, Comparison of 3DSIM thermal modelling of selective laser melting using new dynamic meshing method to ANSYS, Mater. Sci. Technol. 31 (2015) 945–956, http://dx.doi.org/10.1179/1743284714Y.0000000703.

[15] T.A. Krol, M.F. Zaeh, C. Seidel, Optimization of supports in metal-based additive manufacturing by means of finite element models, Solid Free. Fabr. Symp. Austin, TX, 2012.

[16] B. Song, X. Zhao, S. Li, C. Han, Q. Wei, S. Wen, J. Liu, Y. Shi, Differences in microstructure and properties between selective laser melting and traditional

manufacturing for fabrication of metal parts: a review, Front. Mech. Eng. 10 (2015) 111–125, http://dx.doi.org/10.1007/s11465-015-0341-2.
[17] K. Zeng, Optimization of support structures for selective laser melting, Ph.D. Thesis in Industrial Engineering, University of Louisville, 2015.
[18] J.-P. Järvinen, V. Matilainen, X. Li, H. Piili, A. Salminen, I. Mäkelä, O. Nyrhilä, Characterization of effect of support structures in laser additive manufacturing of stainless steel, Phys. Procedia. 56 (2014) 72–81, http://dx.doi.org/10.1016/j.phpro.2014.08.099.
[19] F. Calignano, Design optimization of supports for overhanging structures in aluminum and titanium alloys by selective laser melting, Mater. Des. 64 (2014) 203–213, http://dx.doi.org/10.1016/j.matdes.2014.07.043.
[20] A. Hussein, L. Hao, C. Yan, R. Everson, P. Young, Advanced lattice support structures for metal additive manufacturing, J. Mater. Process. Technol. 213 (2013) 1019–1026, http://dx.doi.org/10.1016/j.jmatprotec.2013.01.020.
[21] G. Strano, L. Hao, R.M. Everson, K.E. Evans, A new approach to the design and optimisation of support structures in additive manufacturing, Int. J. Adv. Manuf. Technol. 66 (2013) 1247–1254, http://dx.doi.org/10.1007/s00170-012-4403-x.
[22] A. Ravindran, K.M. Ragsdell, G.V. Reklaitis, Engineering Optimization: Methods and Applications, Wiley, 2006.
[23] S. Ford, Additive Manufacturing Technology: Potential Implications for U.S. Manufacturing Competitiveness, Social Science Research Network, Rochester, NY, 2014.
[24] W.J. Seufzer, NASA Langley Research Center, Additive Manufacturing Modeling and Simulation A Literature Review for Electron Beam Free Form Fabrication, (2014).
[25] Measurement Science Roadmap for Metal-Based Additive Manufacturing, National Institute of Standards and Technology, 2013.
[26] M.A. Anam, D. Pal, B. Stucker, Modeling and experimental validation of nickel-based super alloy (inconel 625) made using selective laser melting, Proc. Solid Free. Fabr. Symp. Austin, TX, 2013.
[27] T. DebRoy, H.L. Wei, J.S. Zuback, T. Mukherjee, J.W. Elmer, J.O. Milewski, A.M. Beese, A. Wilson-Heid, A. De, W. Zhang, Additive manufacturing of metallic components – process, structure and properties, Prog. Mater. Sci. 92 (2018) 112–224, http://dx.doi.org/10.1016/j.pmatsci.2017.10.001.
[28] M. Garibaldi, I. Ashcroft, M. Simonelli, R. Hague, Metallurgy of high-silicon steel parts produced using selective laser melting, Acta Mater. 110 (2016) 207–216, http://dx.doi.org/10.1016/j.actamat.2016.03.037.
[29] H. Bikas, P. Stavropoulos, G. Chryssolouris, Additive manufacturing methods and modelling approaches: a critical review, Int. J. Adv. Manuf. Technol. 83 (2016) 389–405, http://dx.doi.org/10.1007/s00170-015-7576-2.
[30] W.E. King, A.T. Anderson, R.M. Ferencz, N.E. Hodge, C. Kamath, S.A. Khairallah, A.M. Rubenchik, Laser powder bed fusion additive manufacturing of metals; Physics, computational, and materials challenges, Appl. Phys. Rev. 2 (2015) 041304, http://dx.doi.org/10.1063/1.4937809.
[31] M.M. Francois, A. Sun, W.E. King, N.J. Henson, D. Tourret, C.A. Bronkhorst, N.N. Carlson, C.K. Newman, T. Haut, J. Bakosi, J.W. Gibbs, V. Livescu, S.A. Vander Wiel, A.J. Clarke, M.W. Schraad, T. Blacker, H. Lim, T. Rodgers, S. Owen, F. Abdeljawad, J. Madison, A.T. Anderson, J.-L. Fattebert, R.M. Ferencz, N.E. Hodge, S.A. Khairallah, O. Walton, Modeling of additive manufacturing processes for metals: challenges and opportunities, Curr. Opin. Solid State Mater. Sci. 21 (2017) 198–206, http://dx.doi.org/10.1016/j.cossms.2016.12.001.
[32] K. Zeng, D. Pal, B. Stucker, A review of thermal analysis methods in laser sintering and selective laser melting, 23rd Annu. Int. Solid Free. Fabr. Symp. - Addit. Manuf. Conf. SFF 2012, Austin, TX, 2012, pp. 796–814.
[33] B. Schoinochoritis, D. Chantzis, K. Salonitis, Simulation of metallic powder bed additive manufacturing processes with the finite element method: a critical review, Proc. Inst. Mech. Eng. Part. B J. Eng. Manuf. 231 (2017) 96–117, http://dx.doi.org/10.1177/0954405414567522.
[34] V. Manvatkar, A. De, T. DebRoy, Heat transfer and material flow during laser assisted multi-layer additive manufacturing, J. Appl. Phys. 116 (2014) 124905, http://dx.doi.org/10.1063/1.4896751.
[35] S.A. Khairallah, A. Anderson, Mesoscopic simulation model of selective laser melting of stainless steel powder, J. Mater. Process. Technol. 214 (2014) 2627–2636, http://dx.doi.org/10.1016/j.jmatprotec.2014.06.001.
[36] R. Ammer, M. Markl, U. Ljungblad, C. Körner, U. Rüde, Simulating fast electron beam melting with a parallel thermal free surface lattice boltzmann method, Comput. Math. Appl. 67 (2014) 318–330, http://dx.doi.org/10.1016/j.camwa.2013.10.001.
[37] C. Körner, E. Attar, P. Heinl, Mesoscopic simulation of selective beam melting processes, J. Mater. Process. Technol. 211 (2011) 978–987, http://dx.doi.org/10.1016/j.jmatprotec.2010.12.016.
[38] K. Dai, L. Shaw, Thermal and mechanical finite element modeling of laser forming from metal and ceramic powders, Acta Mater. 52 (2004) 69–80, http://dx.doi.org/10.1016/j.actamat.2003.08.028.
[39] E.R. Denlinger, J. Irwin, P. Michaleris, Thermomechanical modeling of additive manufacturing large parts, J. Manuf. Sci. Eng. 136 (2014) 061007, http://dx.doi.org/10.1115/1.4028669.
[40] R. Paul, S. Anand, F. Gerner, Effect of thermal deformation on part errors in metal powder based additive manufacturing processes, J. Manuf. Sci. Eng. 136 (2014) 031009, http://dx.doi.org/10.1115/1.4026524.
[41] N. Keller, V. Ploshikhin, New method for fast predictions of residual stress and distortion of AM parts, Proc. Solid Free. Fabr. Symp. Austin, TX, 2014.
[42] T.A. Krol, S. Westhäuser, M.F. Zäh, J. Schilp, C. Groth, Development of a simulation-based process chain-strategy for different levels of detail for the preprocessing definitions, Symp. Simulationstechnik, Winterthur, Schweiz, 2011.
[43] W.E. King, H.D. Barth, V.M. Castillo, G.F. Gallegos, J.W. Gibbs, D.E. Hahn, C. Kamath, A.M. Rubenchik, Observation of keyhole-mode laser melting in laser powder-bed fusion additive manufacturing, J. Mater. Process. Technol. 214 (2014) 2915–2925, http://dx.doi.org/10.1016/j.jmatprotec.2014.06.005.
[44] T.A. Krol, M.F. Zah, J. Schilp, C. Seidel, C. Groth, Computational-efficient design of support structures and material modeling for metal-based additive manufacturing, Proc. ANSYS Conf. 29th CADFEM Users Meet. (2011).
[45] M.F. Zaeh, G. Branner, Investigations on residual stresses and deformations in selective laser melting, Prod. Eng. 4 (2010) 35–45, http://dx.doi.org/10.1007/s11740-009-0192-y.
[46] T.A. Krol, C. Seidel, J. Schilp, M. Hofmann, W. Gan, M.F. Zaeh, Verification of structural simulation results of metal-based additive manufacturing by means of neutron diffraction, Phys. Procedia. 41 (2013) 849–857, http://dx.doi.org/10.1016/j.phpro.2013.03.158.
[47] L. Papadakis, A. Loizou, J. Risse, S. Bremen, J. Schrage, a computational reduction model for appraising structural effects in selective laser melting manufacturing: a methodical model reduction proposed for time-efficient finite element analysis of larger components in selective laser melting, Virtual Phys. Prototyp. 9 (2014) 17–25, http://dx.doi.org/10.1080/17452759.2013.868005.
[48] C. Yan, L. Hao, A. Hussein, D. Raymont, Evaluations of cellular lattice structures manufactured using selective laser melting, Int. J. Mach. Tools Manuf. 62 (2012) 32–38, http://dx.doi.org/10.1016/j.ijmachtools.2012.06.002.
[49] I.A. Roberts, Investigation of residual stresses in the laser melting of metal powders in additive layer manufacturing, Ph.D. Thesis, University of Wolverhampton, 2012.
[50] M. Badrossamay, T.H.C. Childs, Further studies in selective laser melting of stainless and tool steel powders, Int. J. Mach. Tools Manuf. 47 (2007) 779–784, http://dx.doi.org/10.1016/j.ijmachtools.2006.09.013.
[51] C. Seidel, M.F. Zaeh, M. Wunderer, J. Weirather, T.A. Krol, M. Ott, Simulation of the laser beam melting process – approaches for an efficient modelling of the beam-material interaction, Procedia CIRP 25 (2014) 146–153, http://dx.doi.org/10.1016/j.procir.2014.10.023.
[52] Thermal Network Modeling Handbook, K&K Associates, 2000.
[53] O.C. Zienkiewicz, R.L. Taylor, The Finite Element Method, 5th ed., Butterworth-Heinemann, Oxford, Boston, 2000.
[54] K. Zeng, D. Pal, C. Teng, B.E. Stucker, Evaluations of effective thermal conductivity of support structures in selective laser melting, Addit. Manuf. 6 (4) (2015) 67–73, http://dx.doi.org/10.1016/j.addma.2015.03.004.
[55] R. LeVeque, Finite Difference Methods for Ordinary and Partial Differential Equations, Society for Industrial and Applied Mathematics, 2007.
[56] M.P. Wand, M.C. Jones, Kernel Smoothing, Taylor & Francis, 1994.
[57] K. Subburaj, S. Patil, B. Ravi, Voxel-based thickness analysis of intricate objects, Int. J. CAD CAM. 6 (2006) 105–115.
[58] R. Paul, S. Anand, Optimization of layered manufacturing process for reducing form errors with minimal support structures, J. Manuf. Syst. 36 (2015) 231–243, http://dx.doi.org/10.1016/j.jmsy.2014.06.014.
[59] N. Keller, F. Neugebauer, H. Xu, V. Ploshikhin, Thermo-Mechanical Simulation of ALM of Titanium Aerospace Structures, Deutsche Gesellschaft für Materialkunde e. V., 2013.
[60] D. Pal, N. Patil, K. Zeng, B. Stucker, An integrated approach to additive manufacturing simulations using physics based, coupled multiscale process modeling, J. Manuf. Sci. Eng. 136 (2014) 061022, http://dx.doi.org/10.1115/1.4028580.
[61] B. Cheng, S. Price, J. Lydon, K. Cooper, K. Chou, On process temperature in powder-bed electron beam additive manufacturing: model development and validation, J. Manuf. Sci. Eng. 136 (2014) 061018, http://dx.doi.org/10.1115/1.4028484.
[62] C. Teng, H. Gong, A. Szabo, J.J.S. Dilip, K. Ashby, S. Zhang, N. Patil, D. Pal, B. Stucker, Simulating melt Pool shape and lack of fusion porosity for selective laser melting of cobalt chromium components, J. Manuf. Sci. Eng. 139 (2017) 011009, http://dx.doi.org/10.1115/1.4034137.
[63] R. Balakrishnan, K. Ranganathan, A Textbook of Graph Theory, Springer, New York, 2012.
[64] Binary STL reader by F. Esmonde-White, MathWorks File Exchange, https://www.mathworks.com/matlabcentral/fileexchange/29906-binary-stl-file-reader, 2011.
[65] S.H. Choi, K.T. Kwok, Hierarchical slice contours for layered-manufacturing, Comput. Ind. 48 (8) (2002) 219–239, http://dx.doi.org/10.1016/S0166-3615(02)00040-4.
[66] S.H. Masood, W. Rattanawong, A generic part orientation system based on volumetric error in Rapid prototyping, Int. J. Adv. Manuf. Technol. 19 (2002) 209–216, http://dx.doi.org/10.1007/s001700200015.
[67] E. Attar, Simulation of Selective Electron Beam Melting Processes, VDM Publishing, 2011.
[68] E. Marin, Characteristic dimensions for heat transfer, Lat.-Am. J. Phys. Educ. 4 (2010) 56–60.